RESEARCH ARTICLE

Receptor-interacting Protein Kinase 2 Is an Immunotherapy Target in Pancreatic Cancer

Wenhua Sang[1], Yiduo Zhou[2], Haiyan Chen[3], Chengxuan Yu[4], Lisi Dai[1], Zhongkun Liu[1], Lang Chen[1], Yimin Fang[4], Panpan Ma[1], Xiangji Wu[5], Hao Kong[5], Wenting Liao[6], Hong Jiang[5], Junbin Qian[2,7,8], Da Wang[4,8], and Yun-Hua Liu[1,8,9]

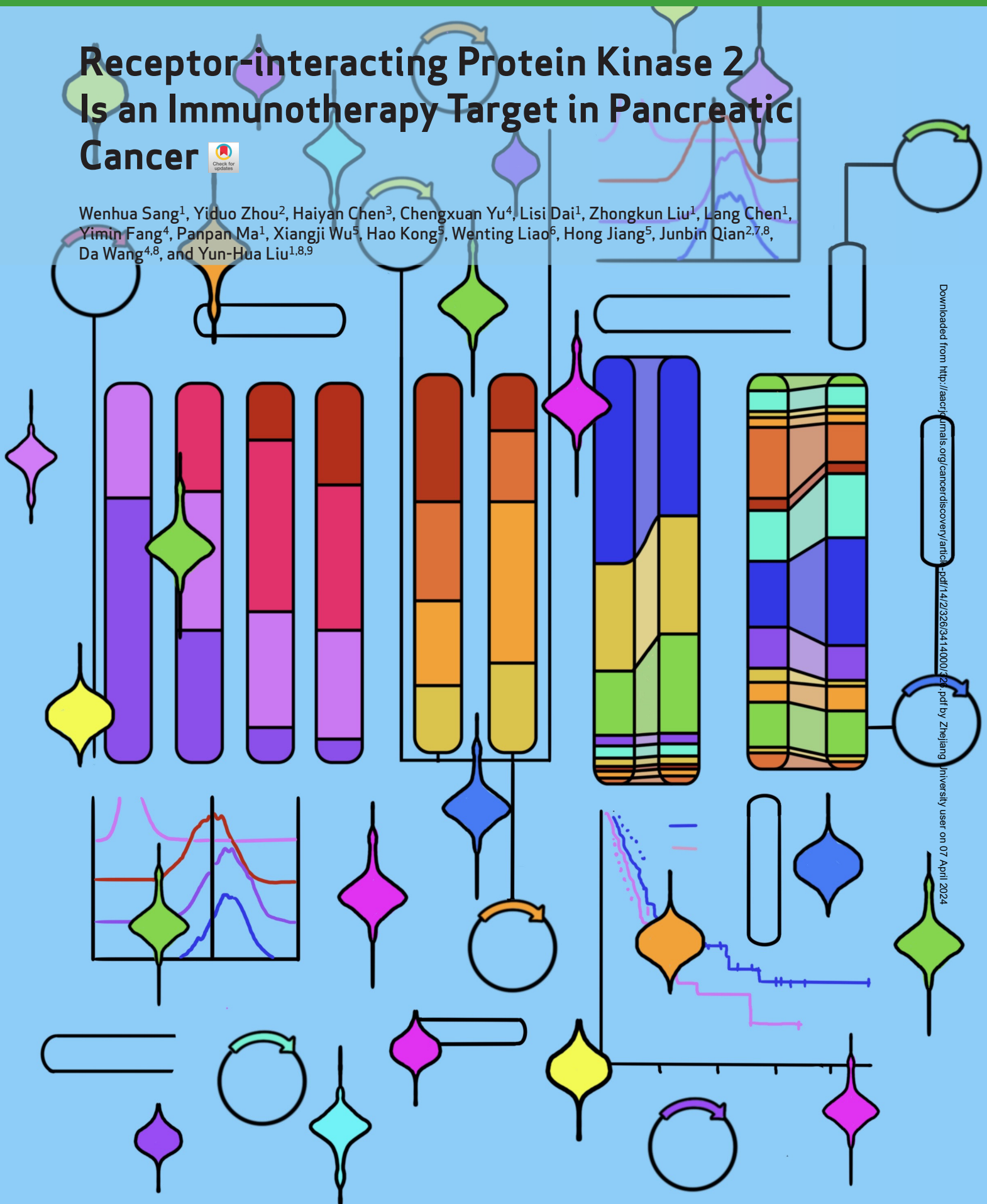

ABSTRACT Pancreatic ductal adenocarcinoma (PDAC) remains a highly lethal malignancy because of its aggressive nature and the paucity of effective treatment options. Almost all registered drugs have proven ineffective in addressing the needs of patients with PDAC. This is the result of a poor understanding of the unique tumor–immune microenvironment (TME) in PDAC. To identify druggable regulators of immunosuppressive TME, we performed a kinome- and membranome-focused CRISPR screening using orthotopic PDAC models. Our data showed that receptor-interacting protein kinase 2 (RIPK2) is a crucial driver of immune evasion of cytotoxic T-cell killing and that genetic or pharmacologic targeting of RIPK2 sensitizes PDAC to anti–programmed cell death protein 1 (anti–PD-1) immunotherapy, leading to prolonged survival or complete regression. Mechanistic studies revealed that tumor-intrinsic RIPK2 ablation disrupts desmoplastic TME and restores MHC class I (MHC-I) surface levels through eliminating NBR1-mediated autophagy-lysosomal degradation. Our results provide a rationale for a novel combination therapy consisting of RIPK2 inhibition and anti–PD-1 immunotherapy for PDAC.

SIGNIFICANCE: PDAC is resistant to almost all available therapies, including immune checkpoint blockade. Through *in vivo* CRISPR screen, we identified that RIPK2 plays a crucial role in facilitating immune evasion by impeding antigen presentation and cytotoxic T-cell killing. Targeting tumor-intrinsic RIPK2 either genetically or pharmacologically improves PDAC to anti–PD-1 immunotherapy.

See related commentary by Liu et al., p. 208.

INTRODUCTION

Pancreatic ductal adenocarcinoma (PDAC) remains a highly aggressive and lethal malignancy, with an average 5-year overall survival rate of less than 10% (1, 2). Over the past decade, immunotherapy, specifically immune checkpoint blockade (ICB), has been shown to boost T cell–mediated immune response. ICB therapy is now emerging as the most promising treatment option for patients with advanced skin, lung, and colorectal cancers (3). Unfortunately, recent clinical trials reported that PDAC is almost uniformly refractory to single-agent ICB and dual-agent ICB with anti-programmed cell death protein 1 (PD-1) and anti–cytotoxic T-cell lymphocyte-4 (CTLA-4) antibodies because of genetic heterogeneity and a highly desmoplastic and immunosuppressive tumor microenvironment (TME; refs. 4–7). This underscores the unmet need for new actionable immune targets to improve PDAC outcomes.

PDAC TME is characterized by a prominent infiltration of myeloid cells that are typically devoid of cytotoxic T lymphocytes (CTL) and low activation markers (e.g., interferon-γ and granzyme B; ref. 5). The lack of robust preexisting T-cell immunity is an essential regulator of disease progression and poor responses to ICB therapy (7). However, the molecular mechanisms regulating PDAC TME and T-cell immunity have yet to be fully understood. Several factors are proposed to limit naturally occurring T-cell immunity, such as low cell surface MHC class I (MHC-I) expression, low mutation burden, and TME-mediated suppression of T-cell priming and function (8, 9). Among them, downregulation of MHC-I–mediated antigen presentation is a primary mechanism by which tumors escape immune surveillance, such as genetic mutations or epigenetic silencing of antigen-processing pathway (APP) genes (10). Consequently, autophagy inhibition to restore tumor cell MHC-I expression or agonistic anti-CD40 antibodies to boost T-cell priming sensitize refractory PDAC to ICB therapy in preclinical models (8, 11, 12). These findings motivated us to discover novel tumor-intrinsic determinants to increase T-cell immunity for PDAC treatment.

Functional genetic screening using CRISPR/Cas9 has proven to be a powerful and unbiased tool for discovering novel immune targets. For example, several flow cytometry–based *in vitro* screens have revealed multiple tumor-intrinsic modulators of programmed death ligand 1 (PD-L1) or MHC-I, which may contribute to immune escape from killing by CTLs (13–16). Using subcutaneous tumor models with a panel of cancer cell lines of different origins, the pooled *in vivo* screens also identified a core set of conserved genes, including *Ptpn2*,

[1]Department of Colorectal Surgery & Oncology of the Second Affiliated Hospital, and Department of Pathology & Pathophysiology, Zhejiang University School of Medicine, Hangzhou, China. [2]Zhejiang Provincial Key Laboratory of Precision Diagnosis and Therapy for Major Gynecological Diseases, Women's Hospital, Zhejiang University School of Medicine, Hangzhou, China. [3]Department of Radiation Oncology, the Second Affiliated Hospital, Zhejiang University School of Medicine, Hangzhou, China. [4]Department of Colorectal Surgery and Oncology, Key Laboratory of Cancer Prevention and Intervention, Ministry of Education, Second Affiliated Hospital, Zhejiang University School of Medicine, Hangzhou, China. [5]Department of Pancreatic Surgery and State Key Laboratory of Biotherapy, West China Hospital, Sichuan University, Chengdu, Sichuan, China. [6]Department of Experimental Research, Sun Yat-sen University Cancer Center, State Key Laboratory of Oncology in South China, Collaborative Innovation Center for Cancer Medicine, Guangzhou, China. [7]Institute of Genetics, Zhejiang University School of Medicine, Hangzhou, China. [8]Zhejiang University Cancer Center, Hangzhou, China. [9]Key Laboratory of Disease Proteomics of Zhejiang Province, Key Laboratory of Cancer Prevention and Intervention of China National Ministry of Education, School of Medicine, Zhejiang University, Hangzhou, China.

W. Sang, Y. Zhou, H. Chen, and C. Yu contributed equally to this article.

Corresponding Authors: Hong Jiang, West China Hospital, Sichuan University, Chengdu, China. E-mail: hjiang@scu.edu.cn; Junbin Qian, Women's Hospital, Zhejiang University School of Medicine, Hangzhou, China. E-mail: dr_qian@zju.edu.cn; Da Wang, Second Affiliated Hospital, Zhejiang University School of Medicine, Hangzhou, China. E-mail: wangda0618@zju.edu.cn; and Yun-Hua Liu, Department of Pathology & Pathophysiology, Zhejiang University School of Medicine, Hangzhou, China. E-mail: yunhualiu@zju.edu.cn

Cancer Discov 2024;14:326–47

doi: 10.1158/2159-8290.CD-23-0584

Setdb1, Pbrm1, Cop1, and *Fitm2*, whose loss could potentiate ICB immunotherapy (17–22). Given the diversity of TMEs in different syngeneic tumor models, these *in vitro* screens or heterotopic skin tumor models do not faithfully capture the complex tumor–immunity interactions within the endogenous TME. Orthotopic tumor models would be a more relevant setting to screen for antitumor immunity targets, but they are technically challenging and may not be feasible for genome-wide screening. Thus, using small, focused libraries is often a more practical strategy for *in vivo* CRISPR screens. However, a focused functional genetic screen using an orthotopic PDAC model has yet to be used to identify biologically relevant immune targets systematically.

In this study, we performed an *in vivo* screening to systematically identify druggable immune targets with a focused library targeting the kinome and membranome (23). Using an orthotopic PDAC model, we found that multiple guide RNAs targeting receptor-interacting protein kinase 2 (RIPK2) were significantly depleted in wild-type mice compared with immunodeficient mice. *Ripk2* encodes a downstream adaptor protein of nuclear oligomerization domain (NOD)-like receptors (NOD1/2) that play a critical role in innate immunity and inflammation (24, 25). Genetic ablation or pharmaceutical inhibition of RIPK2 sensitizes PDAC to ICB therapy, leading to complete or partial regression and prolonged survival. Mechanistically, RIPK2 drives the desmoplastic TME and restricts the activation and density of tumor-infiltrating effector T cells, particularly through inducing NBR1-mediated autophagy–lysosomal degradation of MHC-I. Thus, our studies identified that RIPK2 may be a previously unappreciated immunotherapeutic target, providing a rationale for a novel combination therapy of RIPK2 inhibition and ICB immunotherapy.

RESULTS

In Vivo CRISPR Screens Identify RIPK2 as a Critical Driver of Immune Evasion

To systematically discover tumor-intrinsic determinants whose loss enhances antitumor immunity, we performed a functional CRISPR/Cas9 screening *in vivo* using orthotopic mouse models. KPC^{mut} cells with doxycycline-induced Cas9 expression (KPC^{mut}-Cas9) were transduced with a single-guide RNA (sgRNA) library targeting 2,012 kinase genes and 954 membrane genes (ref. 23; Fig. 1A; Supplementary Fig. S1A and S1B) and then implanted in the parenchyma of pancreas. Tumors were collected after three weeks, and sgRNA representations were evaluated. Using MAGeCK computational algorithms (15, 19), we ranked sgRNAs that were depleted or enriched in C57BL/6 hosts (immunocompetent) compared with nude mice (immunodeficient; Supplementary Fig. S1C–S1E). Multiple known mediators of immune evasion [*Cdk6*, *Ptpn2*, *Ptk2* (encoding FAK) and *Cd47*] and key components of the IFNγ response pathway (*Jak1*) were significantly depleted in wild-type mice, validating the robustness of our screens (Fig. 1B; Supplementary Table S1). Notably, *Ripk2*, which encodes a kinase serving as the signaling adaptor protein for the NOD1/2 intracellular receptors that recognize intracellular bacteria, emerged as the top-ranked depleted gene in KPC^{mut} tumors of immunocompetent mice relative to nude mice.

In validation experiments, we genetically knocked down *Ripk2* with short hairpin RNAs (shRNA: shRipk2–1 and shRipk2–2) in three murine PDAC cell lines (KC6141, KPC^{mut}, and KPC^{flox}) derived from *Pdx1-Cre;LSL-Kras*^{G12D}*;LSL-Trp53*$^{R172H/+}$ (KPC^{mut}) or *Pdx1-Cre;LSL-Kras*^{G12D}*;Trp53*$^{flox/flox}$ (KPC^{flox}) mouse models (26, 27). *Ripk2* knockdown has no noticeable effect on cell proliferation *in vitro* compared with nontargeting control (Supplementary Fig. S2A–S2D). These cells were inoculated in parallel into immunodeficient mice and syngeneic wild-type hosts. Both subcutaneous and orthotopic inoculations were used to assess tumor growth. We observed that genetic depletion of RIPK2 resulted in a modest reduction in tumor growth in nude mice bearing shRipk2 and scramble (shNT) KC6141 tumors (s.c.; Fig. 1C and D). In contrast, *Ripk2* knockdown dramatically impaired tumor growth and extended survival in immunocompetent mice (Fig. 1E and F; Supplementary Fig. S2E–S2G). Similarly, *Ripk2* knockdown significantly reduced tumor growth in C57BL/6 mice bearing KPC^{mut} or KPC^{flox} tumors but comparable tumor growth in nude mice (Supplementary Fig. S2H–S2L). To further validate these results, we knocked out *Ripk2* with CRISPR/Cas9 technology and conducted similar experiments (Supplementary Fig. S2M). Again, knocking out *Ripk2* markedly blunted KPC^{mut} tumor progression and led to almost complete tumor regression (5 or 6 of 6 mice) without any signs of residual tumors or liver metastases 180 days after implantation (Fig. 1G and H; Supplementary Fig. S2N–S2P). However, *Ripk2* knockdown resulted in similar tumor progression in nude mice (Fig. 1I and J). To further delineate whether cytotoxic CD8$^+$ T cells were essential for shRipk2-mediated tumor inhibition, we depleted CD4$^+$ or CD8$^+$ T cells in tumor-bearing mice using neutralizing antibodies. When CD8$^+$ T cells were depleted, *RIPK2* depletion–induced reduction in tumor weight was completely offset (Supplementary Fig. S2Q–S2S). These results indicate that tumor-intrinsic RIPK2 may be a novel modulator of adaptive immunity that supports tumor progression.

RIPK2 is Overexpressed in Human PDAC and Correlates with Poor Patient Survival

Given the pronounced potency of RIPK2 in driving PDAC immune evasion, we evaluated RIPK2 expression by IHC in a

Figure 1. *In vivo* CRISPR screens identify RIPK2 as a critical driver of immune evasion. **A,** Workflow of *in vivo* CRISPR screens to identify the potential therapeutic targets in PDAC immune evasion. **B,** MAGeCK analysis and robust rank aggregation (RRA) ranking of top depleted genes in immunocompetent (B6) versus immunodeficient (nude) hosts in the *in vivo* CRISPR screens. **C** and **D,** Effect of *Ripk2* knockdown on subcutaneously implanted KC6141 tumor growth in nude mice. Tumor weight, image (**C**), and tumor volume (**D**) are shown. Mean ± SD, $n = 5$–6 per group. Two-tailed *t* test (**C**) and two-way ANOVA (**D**). **E** and **F,** Effect of *Ripk2* knockdown on subcutaneously (sc) implanted KC6141 tumor growth in wild-type C57BL/6 mice. Tumor volume (**E**), weight, and image (**F**) are shown. Mean ± SD, $n = 8$ per group. Two-way ANOVA (**E**) and two-tailed *t* test (**F**). **G** and **H,** Effect of *Ripk2* knockout on orthotopically implanted KPC^{mut} tumor growth in wild-type C57BL/6 mice. Kaplan–Meier survival analysis (**G**) of host animals bearing scramble control and *Ripk2*-KO KPC^{mut} tumors. End-stage pancreas weight is shown in **H**. Mean ± SD, $n = 6$ per group. Log-rank Mantel–Cox test (**G**) and two-tailed *t* test (**H**). **I** and **J,** Effect of *Ripk2* knockout on subcutaneously implanted KPC^{mut} tumor growth in nude mice. Tumor volume (**I**) and weight (**J**) are shown. Mean ± SD, $n = 8$ per group. Two-way ANOVA (**I**) and two-tailed *t* test (**J**).

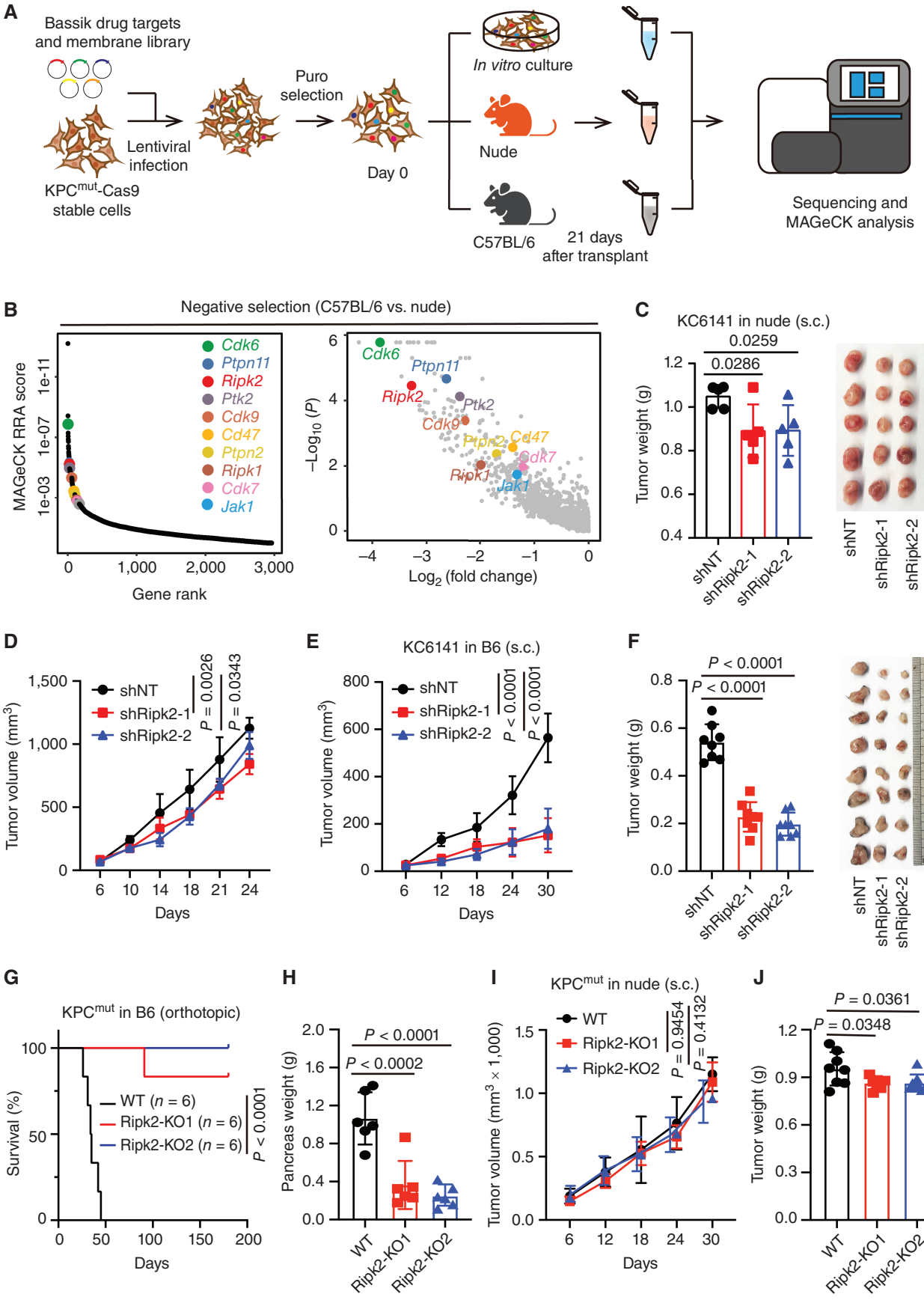

human tissue microarray (TMA) containing 60 PDAC tumors and 10 normal pancreatic tissues (Supplementary Table S2). In contrast to the normal pancreatic epithelium, RIPK2 was detectable in early pancreatic intraepithelial neoplasia lesions (PanIN) and was modestly upregulated in late PanINs and substantially elevated in PDAC lesions (Fig. 2A and B; Supplementary Fig. S3A). However, RIPK2 expression did not correlate with sex or age (Supplementary Fig. S3B). Similarly, we also analyzed RIPK2 expression in pancreatic tissues from the *p48-Cre;LSL-Kras*^{G12D}*;Tgfbr2*$^{flox/flox}$ (KTC; ref. 28) or KPC^{flox} mouse models and found that its expression was positively correlated with tumor progression (Supplementary Fig. S3C and S3D). Moreover, although RIPK2 expression in neighboring stroma cells (mainly fibroblasts and macrophages) was detectable, malignant PDAC cells expressed much higher levels of RIPK2, consistent with previous single-cell transcriptome studies (ref. 29; Supplementary Fig. S3E and S3F).

Bioinformatic analysis of the Cancer Genome Atlas (TCGA) and GSE16515 datasets (30) found that RIPK2 was highly amplified (4.2%, 7/168) or gained (28.0%, 47/168) in PDAC (Supplementary Fig. S3G). Therefore, its expression was significantly increased compared with normal pancreatic tissue, correlated with poor disease-free and overall survival in human PDAC cohort (Fig. 2C–F). Transcriptome analysis demonstrated that RIPK2 expression was enriched in basal-like tumors and associated with activated stromal subtype (ref. 31; Supplementary Fig. S3H–S3J). Given RIPK2 expression is positively correlated with KRAS (Fig. 2G), the primary driver of PDAC tumorigenesis, we validated this correlation using a couple of iKras cell lines derived from the inducible model of PDAC (32). *Ripk2* mRNA expression is approximately 2-fold higher in *Kras*^{G12D}-ON compared with *Kras*^{G12D}-OFF (72 hours) samples, which was further validated by Western blot analysis showing a loss of RIPK2 expression after abolishing *Kras*^{G12D} signaling (Fig. 2H and I; Supplementary Fig. S3K and S3L). To determine whether RIPK2 overexpression is relevant for desmoplastic and immunosuppressive TME, we evaluated collagen deposition (Masson trichrome) and tumor-infiltrating CD8$^+$ T cells (IHC) in human PDAC tissue arrays. The intensity and area of RIPK2 were used to stratify our cohort into the RIPK2-high and RIPK2-low groups. We observed that high levels of RIPK2 in tumor cells were associated with fewer infiltrated CD8$^+$ T cells but higher levels of collagen deposition (Fig. 2J–M). Together, these data suggest that overexpression of RIPK2 in tumor cells correlates well with fibrotic and immunosuppressive TME and poor patient survival.

RIPK2 Modulates the Immune Profile and Impairs Antitumor T-cell Response

To uncover the immune mechanism by which tumor-intrinsic loss of RIPK2 can drive immune evasion, we analyzed end-stage orthotopic tumors derived from KPC^{mut} cells. As the complete loss of RIPK2 almost uniformly abrogated KPC^{mut} tumor initial establishment, *Ripk2* knockout tumors did not reach an appropriate size for immune phenotyping analysis (Fig. 1G and H). Therefore, only *Ripk2* knockdown tumors (shRipk2) were chosen for subsequent experiments. We found that RIPK2 ablation significantly decreased collagen deposition (Masson trichrome) cancer-associated fibroblast (CAF) activation [expressing fibroblast activation protein alpha (FAP) or α-smooth muscle actin (α-SMA) and proliferation (Ki-67) but not the total number of fibroblasts (expressing podoplanin (PDPN); Supplementary Fig. S4A–S4H]. Similar differences were observed in KPC^{flox} tumors. However, when CD8$^+$ T cells, but not CD4$^+$ T cells, were depleted, RIPK2 ablation–induced reduction in CAF activation and proliferation was largely abrogated (Supplementary Fig. S4I and S4J), suggesting that the difference in tumor growth by RIPK2 deficiency was unlikely to be explained by changes in desmoplasia.

To understand how RIPK2 depletion could alter the immune landscape of PDAC tissues, we used a single-cell RNA sequencing (scRNA-seq) of tumor-infiltrating CD45$^+$ leukocytes from KPC^{mut} tumors to map the tumor–immune transcriptional landscape in an unbiased manner. After quality control, we obtained single-cell transcriptomes of 29,448 cells isolated from shRipk2 and shNT tumors. The uniform manifold approximation and projection (UMAP) algorithm was used to determine the distribution of cellular clusters, and their identities were annotated on the basis of the expression of known marker genes (Fig. 3A; Supplementary Fig. S5A). We observed a significant expansion of lymphocyte clusters and contraction of granulocytic cell clusters in shRipk2 tumors, whereas the proportions of F4/80$^+$ tumor-associated macrophages (TAM) and CD4$^+$FOXP3$^+$ regulatory T cells (Treg) were comparable between conditions (Fig. 3A). Recluster analysis on 4,533 T and natural killer (NK) cells from both groups identified 14 subclusters, including 5 CD4$^+$ T-cell (C1–C5), 5 CD8$^+$ T-cell (C6–C10), 2 γδT cell (C11–C12), 1 NK-cell, and 1 innate lymphoid cell clusters (Fig. 3B; Supplementary Fig. S5B). Notably, the dramatic increase in T-cell proportion in shRipk2 tumors was driven almost entirely by experienced CD8$^+$ T cells (T_{EX} cells) and effector/memory CD8$^+$ T cells (T_{EM} cells) (Fig. 3B; Supplementary Fig. S5C). The T_{EX} cells represent activated T cells with exhaustion-like characteristics based on the expression of immune checkpoint (*Lag3, Pdcd1*), effector (*Ifng, Nkg7*), and cytotoxic (*Gzmb, Prf1*) markers (Supplementary Fig. S5B). Next, we computationally imputed pseudotime trajectories using Slingshot with naive T cells (T_N cells) as the root state. Consistent with our previous studies (33), T_N cells were connected to T_{EM} and T_{EX} cells, which then branched into two different trajectories to form cytotoxic CD8$^+$ T cells (characterized by high expression of *Gzmd*, $T_{EX\text{-}GZMD}$) and memory/stem T cells (characterized by high expression of *Ccr7*, T_{SCM}; Fig. 3C). Although the trajectories allocate cells with a similar expression to the same pseudotime, we observed that CD8$^+$ T cells from shRipk2 tumors expressed effector and cytotoxic activity–related genes (*Cd69, Gzmb, Gzmk*, and *Ifngr1*) at significantly higher levels than shNT tumors (Fig. 3D). However, the expression levels of exhaustion markers, including *Ctla4*, *Pdcd1*, *Lag3*, and *Havcr2*, were comparable between two groups (Supplementary Fig. S5D). We used gene set enrichment analysis (GSEA) to find differentially represented pathways in CD8$^+$ T cells between shRipk2 and shNT groups. CD8$^+$ T cells from shRipk2 tumors were enriched for various pathways related to T-cell activities, such as T-cell activation, proliferation, killing, and antigen receptor–mediated signaling (Fig. 3E).

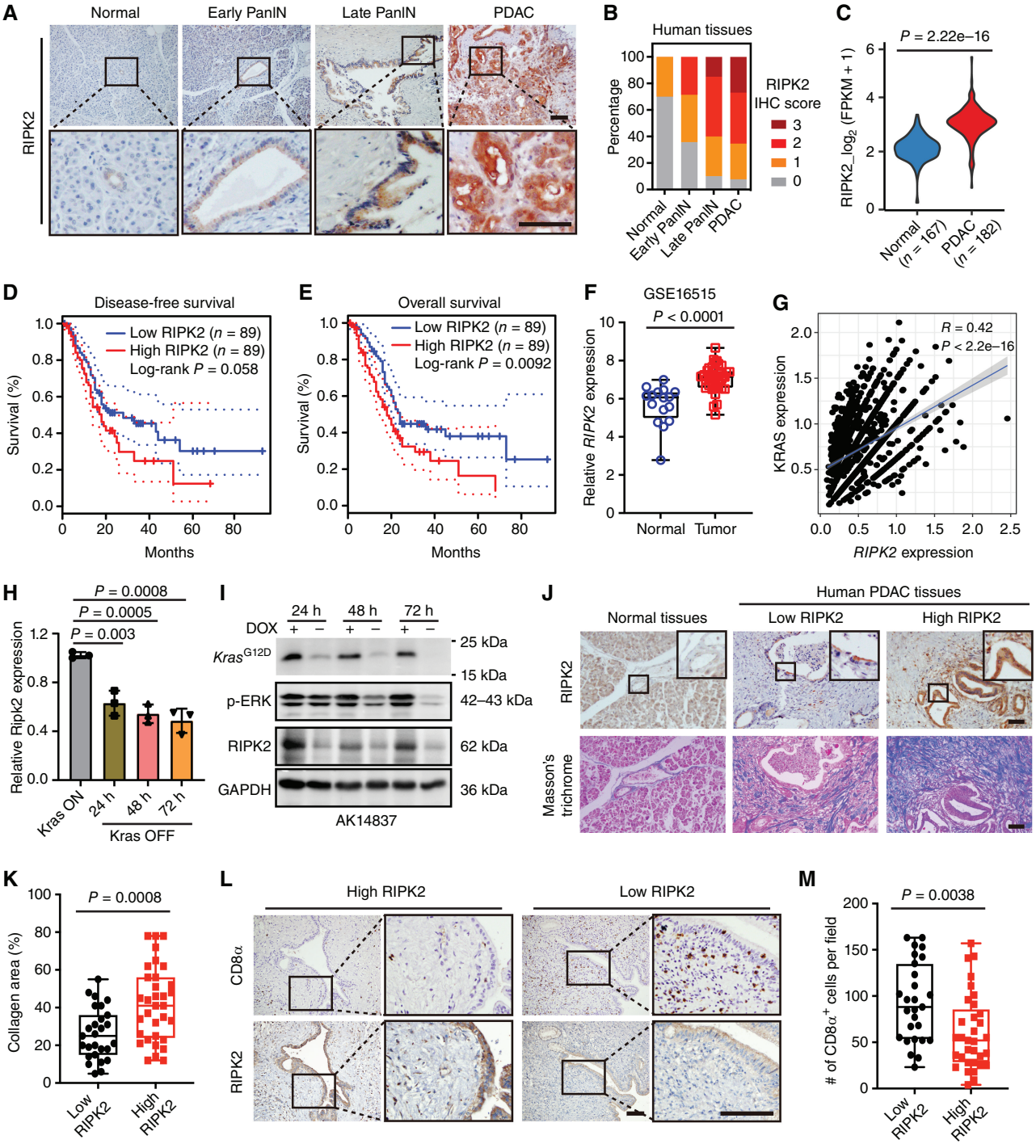

Figure 2. RIPK2 is overexpressed in human PDAC and correlates with poor patient survival. **A,** Representative IHC analysis for RIPK2 expression in human normal pancreatic tissues and early PanIN, late PanIN, and PDAC tumor tissues. Scale bars, 50 μm. **B,** Quantification of RIPK2 expression in human normal pancreatic tissues ($n = 10$), early PanIN ($n = 14$), late PanIN ($n = 20$), and PDAC ($n = 26$) tissues by deterring RIPK2 IHC score. **C,** *RIPK2* mRNA expression in normal pancreatic tissues ($n = 167$) and PDAC tissues ($n = 182$) in TCGA datasets. Wilcoxon rank-sum test. **D** and **E,** Disease-free survival (**D**) and overall survival (**E**) were analyzed and compared between patients with low ($n = 89$) and high ($n = 89$) expression levels of RIPK2 in TCGA PDAC dataset from the GEPIA web portal. Log-rank Mantel–Cox test. **F,** *RIPK2* mRNA expression in normal pancreatic tissues ($n = 16$) and PDAC tissues ($n = 36$) in the GSE16515 dataset. Two-tailed *t* test. **G,** The correlation of *RIPK2* mRNA expression with that of *KRAS* in TCGA PDAC dataset from the GEPIA web portal. qRT-PCR (**H**) and Western blot (**I**) analyses of *Ripk2* mRNA and protein expression in the Kras ON and OFF AK14837 cell line. Representative RIPK2 IHC and Masson trichrome staining in human normal pancreas and PDAC tissues (**J**). Collagen deposition (**K**) was compared between patients with low ($n = 27$) and high ($n = 33$) expression levels of RIPK2. Two-tailed *t* test. Scale bars, 50 μm. Representative RIPK2 and CD8α IHC staining in human PDAC tissues (**L**). Quantification of $CD8^+$ cells per field was compared between patients with low ($n = 27$) and high ($n = 33$) expression levels of RIPK2 (**M**). Two-tailed *t* test and scale bars, 50 μm.

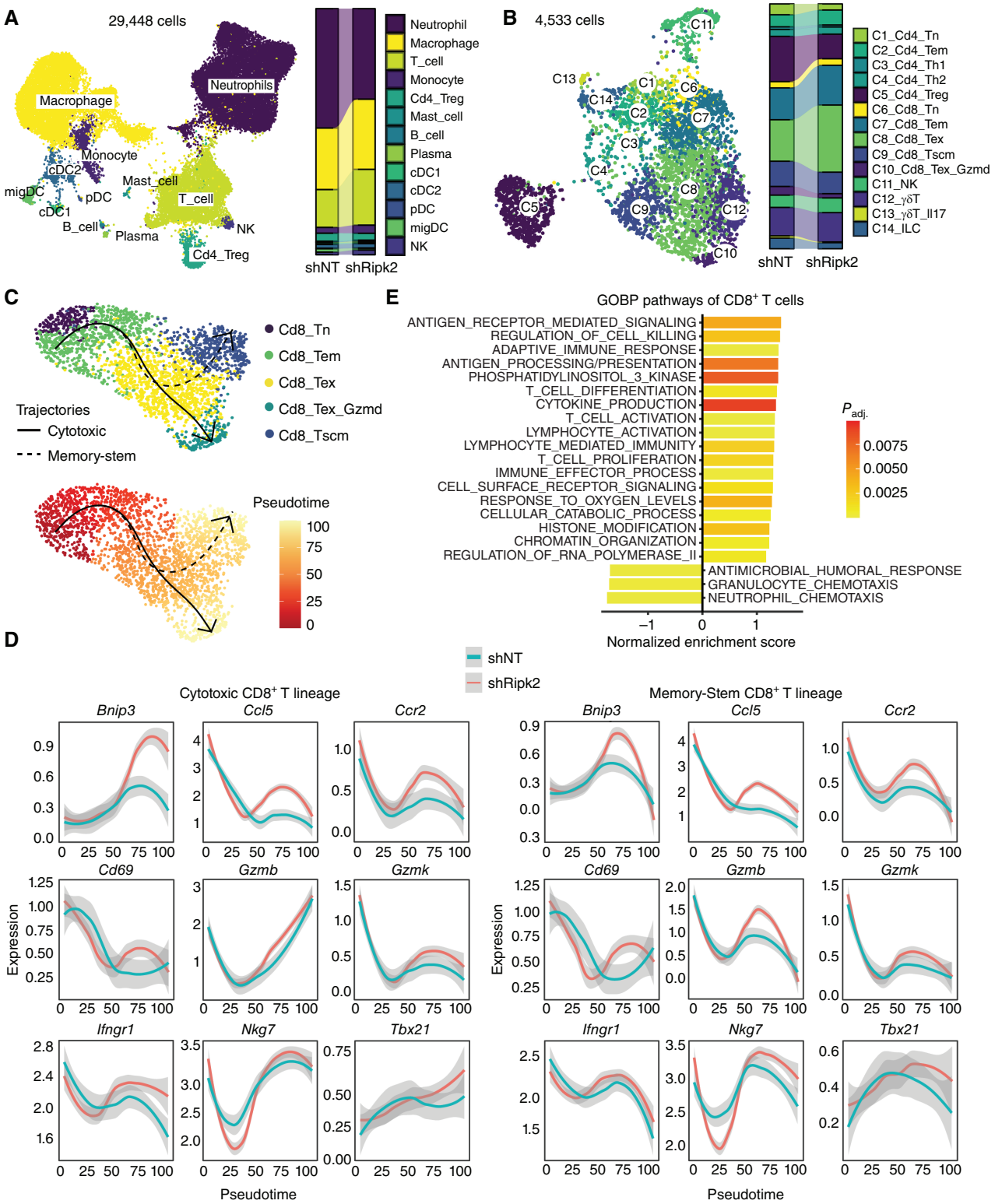

Figure 3. RIPK2 modulates the immune profile and impairs antitumor T-cell response. **A,** scRNA-seq was performed on all live leukocytes (PI^-, $CD45^+$) in shNT and shRipk2 KPC^{mut} tumors harvested on day 21. UMAP plot shows the distribution of clusters, colored by annotated cell type combined from both groups, and the relative fraction of each cluster was shown on the right. $n = 3$ tumors pooled/group. **B,** UMAP plot of 4,533 T and NK cells combined from shNT and shRipk2 KPC^{mut} tumors colored by annotated cell type, and relative fraction of each cluster were shown. $n = 3$ tumors pooled/group. **C** and **D,** Pseudotime trajectories for $CD8^+$ T cells based on Slingshot, showing two trajectories (T_{SCM} and $T_{EX\text{-}GZMD}$), color-coded for $CD8^+$ T-cell phenotypes (**C**, top) and pseudotime (**C**, bottom). Plot of markers and functional genes along the $CD8^+$ T-cell trajectories (**D**). **E,** Canonical pathway perturbations scored by gene-set enrichment analysis (GSEA) in reclustered $CD8^+$ T cells from shRipk2 versus shNT tumors. (*continued on following page*)

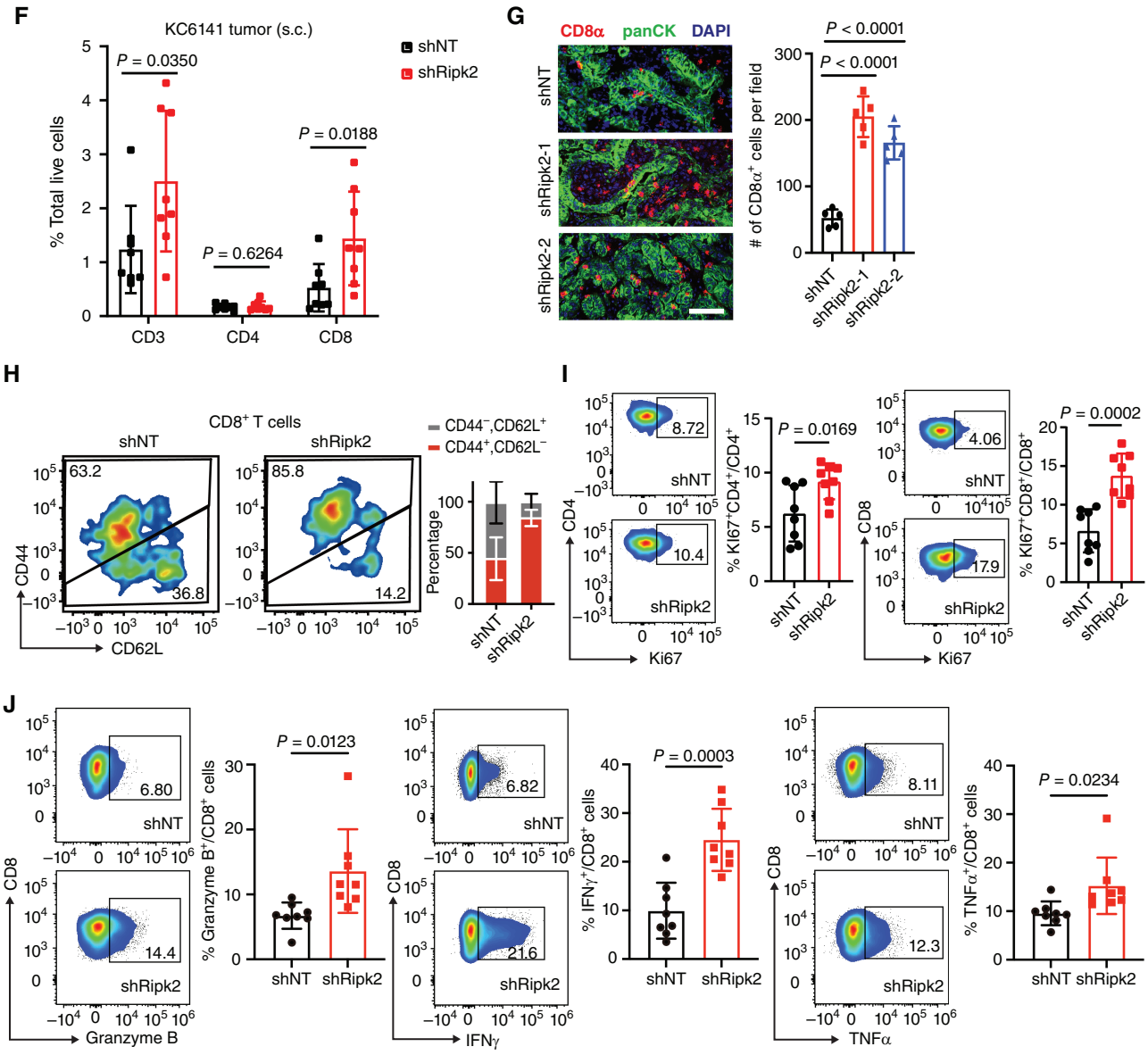

Figure 3. ***(Continued)*** **F,** Flow cytometry analysis of subcutaneously implanted shNT and shRipk2 KC6141 tumors. The percentage of CD3+, CD8+, and CD4+ T cells in tumors was analyzed. Mean ± SD, $n = 8$ per group, two-tailed t test. **G,** Representative immunofluorescence staining for CD8α and pan-keratin (panCK) in end-stage shNT and shRipk2 KPC^{mut} tumor tissues. The number of CD8+ cells per field was quantified. Mean ± SD, $n = 5$ biological replicates, two-tailed t test. Scale bar, 50 μm. **H** and **I,** Flow cytometry analysis of intratumoral CD8+ and CD4+ T-cell subsets in end-stage shNT and shRipk2 KPC^{mut} tumor tissues without restimulation. Mean ± SD, $n = 4$–8 per group, two-tailed t test. **J,** Percentages of tumor-infiltrating IFNγ+, TNFα+, and granzyme B+ CD8+ T cells were analyzed by flow cytometry after restimulation. Mean ± SD, $n = 8$ per group, two-tailed t test.

To validate the enhanced density and functionality of CD8+ T cells from shRipk2 tumors, flow cytometry was used to profile immune cell subsets in both KC6141 and KPC^{mut} tumors. In both syngeneic models, Ripk2-deficient tumors, but not spleen or tumor-draining lymph node (dLN), had increased CD3+ and CD8+ T cells regardless of whether they were a fraction of CD45+ leukocyte infiltrates or total live cells (Fig. 3F; Supplementary Fig. S5E and S5F). Using immunofluorescence staining, we confirmed a significant increase in tumor-infiltrating CD8+ T cells in end-stage shRipk2 KPC^{mut} and KPC^{flox} tumors compared with shNT controls (Fig. 3G; Supplementary Fig. S5G). We also found a significant proportion of CD4+ and CD8+ T cells from shRipk2 tumors exhibited an effector phenotype (CD44+ CD62L−) and only a minority was naïve (CD44− CD62L+; Fig. 3H; Supplementary Fig. S5H). More importantly, RIPK2 ablation in tumor cells not only promoted intratumor CD8+ T-cell proliferation (Fig. 3I; Supplementary Fig. S5I), based on Ki-67 levels, but augmented the production of cytolytic granules Granzyme B and cytokines (IFNγ, TNFα) in tumor-infiltrating CD8+ T cells (Fig. 3J), indicating increased functionality and active state of these cells.

In addition to lymphocyte clusters, we also validated the effects of RIPK2 deficiency on other immune cell populations

in KPC^{mut} tumors. The percentage of NK cells and CD103$^+$ dendritic cells (DC) in tumors increased with depletion of RIPK2 (Supplementary Fig. S5J and S5K). Although the ratio of granulocytic MDSC (G-MDSC) (CD11b$^+$Ly6G$^+$Ly6c^{low}), monocytic MDSC (M-MDSC) (CD11b$^+$Ly6G$^-$Ly6C^{high}), and macrophages (CD11b$^+$F4/80$^+$) to tumor cells was largely similar between conditions (Supplementary Fig. S5J and S5K), RIPK2 ablation reprogrammed TAMs toward an immunogenic M1-like phenotype, including a modest upregulation of MHC-II and TNFα with a concomitant reduction in CD206, Arg1, and IL10 (Supplementary Fig. S5L–S5N). However, the expression of Gr1 and S100A9 was comparable between shRipk2 and shNT tumors (Supplementary Fig. S5O and S5P). Concordantly, further clustering of monocytes/macrophages gave rise to 8 subpopulations. RIPK2 ablation increased the proportion of proinflammatory TAMs (*Ccl5*$^+$, *Nr4a2*$^+$ and *C1qc*$^+$) but decreased the proportion of anti-inflammatory TAMs (*Spp1*$^+$, *Lyve1*$^+$, and *Retnla*$^+$; Supplementary Fig. S5Q–S5U). These findings imply that CD8$^+$ T cells are the immune cell type in PDAC TME most dramatically impacted by RIPK2 deficiency.

RIPK2 Restricts the Activation and Effector States of CD8$^+$ T Cells by Impairing Antigen Presentation

To determine whether RIPK2 expression in tumor cells directly affects the activation and effector states of CD8$^+$ T cells, we cocultured ovalbumin (OVA)-expressing KPC^{mut} cells with CD8$^+$ T cells isolated from OT-I transgenic mice, whose T-cell receptor (TCR) is known to react with the ovalbumin peptide 257–264. After coculture overnight, we validated the activation of naive T cells based on their expression of CD69 (a known marker of T-cell priming) and the production of cytokines (Fig. 4A and B). Whereas coculture with control tumor cells resulted in minimal or delayed T-cell activation, rapid T-cell activation was evident for cells cocultured with *Ripk2* knockout KPC^{mut}-OVA cells. Specifically, OT-I T cells cocultured with *Ripk2* knockout tumor cells exhibited strong expression of CD69 and higher production of TNFα, IFNγ, and granzyme B (Fig. 4A and B). Furthermore, when cocultured with activated OT-I T cells, shRipk2-expressing cells were more vulnerable to CD8$^+$ T cell–mediated killing than control KC6141-OVA or KPC^{mut}-OVA cells (Fig. 4C; Supplementary Fig. S6A). Notably, these effects were MHC-I specific because an H-2K^b-SIINFEKL blocking antibody inhibited OT-I cell proliferation (Fig. 4D; Supplementary Fig. S6B), suggesting that MHC-I–mediated antigen presentation could be involved in the function of RIPK2.

Given that CD8$^+$ T-cell activation is mediated by the engagement of TCR to the antigen-derived peptide–MHC-I complex, we hypothesized that RIPK2 might influence antigen presentation on the surface of tumor cells. Indeed, we detected that the staining of H-2K^b molecules bound to SIINFEKL was significantly increased in shRipk2-expressing mouse PDAC cells compared with scramble controls (Fig. 4E). Similarly, *RIPK2* knockdown also boosted the surface levels of class I HLA in multiple human PDAC cell lines (Fig. 4F; Supplementary Fig. S6C and S6D). This difference in antigen presentation was further amplified in the presence of IFNγ stimulation. We also observed increased levels of class I HLA in human PDAC cell lines after doxycycline-induced *RIPK2* silencing (Supplementary Fig. S6E and S6F). Furthermore, by immunofluorescence (IF), class I HLA staining indicated a greater localization to the plasma membrane in *RIPK2*-depleted PANC-1 and HPAC cells (Fig. 4G; Supplementary Fig. S6G). In contrast, RIPK2 deficiency failed to show any effect on PD-L1 expression and had only a marginal impact on MHC-II expression in both human and mouse PDAC cells (Supplementary Fig. S6H and S6I).

In accordance with these *in vitro* results, the surface levels of H-2K^b, but not PD-L1, on orthotopically implanted shRipk2-expressing KPC^{mut} and KPC^{flox} tumor cells were also increased when compared with shNT controls (Fig. 4H; Supplementary Fig. S6J and S6K). To further confirm the effect of increased MHC-I expression after *Ripk2* knockdown on tumor growth *in vivo*, cell surface levels of H-2K^b were depleted by knocking down *H2-K1* gene. *H2-K1* knockdown led to loss of MHC-I expression *in vivo*, rescued retarded shRipk2 tumor growth, and decreased the number of CD8$^+$ T cells in shRipk2-expressing tumors (Fig. 4I–L; Supplementary Fig. S6L). Collectively, these results indicate that tumor-intrinsic RIPK2 functions as a suppressive molecule that restricts T-cell activation and effector states through impairing MHC-I expression.

RIPK2 Promotes MHC-I Trafficking to Lysosomes via NBR1

We then explored how MHC-I expression was boosted in PDAC tumor cells after RIPK2 depletion. Given that MHC-I is often regulated by cell-extrinsic autocrine, we compared shNT and shRipk2 cells cultured in conditional medium

Figure 4. RIPK2 restricts the activation and effector states of CD8$^+$ T cells by impairing antigen presentation. Quantification of CD69$^+$ (**A**, $n = 4$ per group) and IFNγ$^+$, TNFα$^+$, and granzyme B$^+$ (**B**, $n = 5$ per group) CD8$^+$ T cells by flow cytometry. Naive OT-I T cells were cocultured with shNT/shRipk2-expressing KPC^{mut}-OVA cells at a ratio of 2.5:1 (T cell: KPC^{mut}-OVA cells) for 24 hours. Mean ± SD, two-tailed *t* test. **C,** *In vitro* cytotoxicity assays for activated OT-I T cells against *Ripk2* knockdown or control KC6141-OVA cells. Mean ± SD, $n = 3$ per group, two-tailed *t* test. **D,** Coculture of naive OT-I cells with KPC^{mut}-OVA cells in the presence of H-2K^b-SIINFEKL or IgG control antibodies for 48 hours. OT-I proliferation was measured by 5-(and-6)-Carboxyfluorescein diacetate N-succinimidyl ester (CFSE) dilution. Mean ± SD, $n = 5$ per group, two-tailed *t* test. **E,** H-2K^b expression levels were determined by flow cytometry in control or RIPK2-deficient KC6141 cells. Mean ± SD, $n = 4$ per group, two-tailed *t* test. **F,** Class I HLA expression levels were determined by flow cytometry in control or *RIPK2*-deficient PANC-1 cells upon IFNγ stimulation for 24 hours. Mean ± SD, $n = 3$ per group, two-tailed *t* test. **G,** Representative confocal images of class I HLA distribution in control or *RIPK2*-deficient PANC-1 cells. WGA, wheat germ agglutinin (a marker of plasma membrane). Quantification of colocalization of class I HLA with WGA on plasma membrane is shown in the right panel. Mean ± SD, $n = 3$ biological replicates (10 fields), two-tailed *t* test. Scale bar, 5 μm. **H,** Quantification of H-2K^b expression levels in EpCAM$^+$ KPC^{mut} tumor cells by flow cytometry. shNT/shRipk2 KPC^{mut} cells were orthotopically implanted into C57BL/6 mice, and tumors were harvested on days 21–25 after inoculation. Mean ± SD, $n = 3$ biological replicates, two-tailed *t* test. **I–L,** Effect of *Ripk2* knockdown on subcutaneously implanted shNT or shH2k1 KPC^{mut} tumor growth in wild-type C57BL/6 mice. Tumor volume (**I**), image (**J**), weight (**K**), and quantification of infiltrating CD8$^+$ T cells per field (**L**) are shown. Mean ± SD, $n = 6$ per group, two-way ANOVA (**I**), and two-tailed *t* test (**K** and **L**).

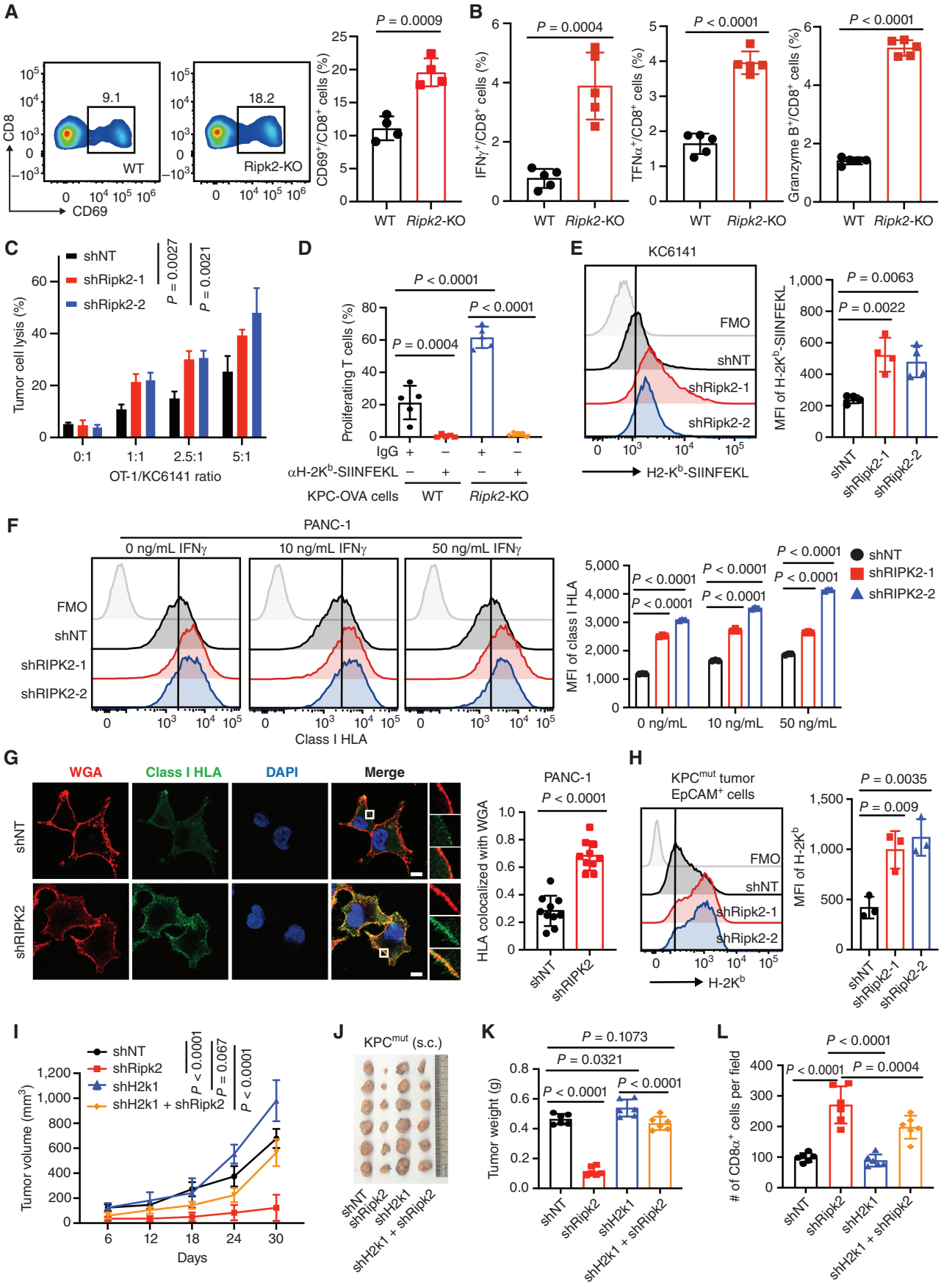

from shNT control or shRipk2 cells. Although *Ripk2* knockdown upregulates surface levels in KPC^{mut} tumor cells, no significant differences were observed between different media conditions (Supplementary Fig. S7A and S7B), suggesting that tumor-intrinsic RIPK2 modulates MHC-I in a cell-autonomous manner. Moreover, we detected comparable levels of *HLA-A/B/C* as well as MHC-I APP transcripts in shNT control and shRIPK2 cells, indicating that RIPK2 may regulate MHC-I protein stability rather than mRNA transcripts (Supplementary Fig. S7C and S7D). To test this possibility, we evaluated the half-life of MHC-I in human PDAC cells by blocking *de novo* protein synthesis. Upon cycloheximide treatment, the levels of class I HLA in PANC-1 and CFPAC-1 cells bearing shRipk2 declined more slowly than in control cells (Fig. 5A; Supplementary Fig. S7E). This suggests that ablation of RIPK2 in tumor cells impairs MHC-I degradation, leading to elevated MHC-I protein stability.

Membrane proteins, including MHC-I, are often transported and degraded in the lysosome and/or proteasome. We treated PANC-1 and CFPAC-1 cells with V-ATPase inhibitor bafilomycin (BafA1) to inhibit lysosome function. Class I HLA levels increased substantially in control cells but did not change much in *RIPK2* knockdown cells (Fig. 5B; Supplementary Fig. S7F), suggesting a crucial role for RIPK2 in regulating class I HLA levels through lysosome-mediated degradation. Furthermore, we performed immunofluorescence staining for LAMP1 (a lysosome marker) and LC3 (an autophagosome marker) in PANC-1 and HPAC-1 cells. As expected, loss of RIPK2 dramatically decreased class I HLA localization in lysosome and autophagosome, as shown by costaining of class I HLA with LAMP1 or LC3 puncta, respectively (Fig. 5C and D; Supplementary Fig. S7G and S7H). Immunoblotting results showed that loss of RIPK2 led to decreased LC3-II levels, which was fully reversed by treatment with BafA1, which blocks the degradation of autophagosomes (Fig. 5E; Supplementary Fig. S7I). This indicates that ablation of RIPK2 may mainly alter autophagosome synthesis, thus inhibiting the degradation of MHC-I.

Previous studies have found that RIPK2 is an adapter kinase that regulates innate immune signaling by interacting with several proteins. To identify potential interaction binding partners of RIPK2 and MHC-I, we performed immunoprecipitation coupled with mass spectrometry (IP-MS) experiments. Interestingly, we detected that NBR1 was one of the most abundant subunits in RIPK2 immunoprecipitates (Supplementary Fig. S7J). NBR1 is an autophagy receptor and has been shown to interact with and target ubiquitylated substrates, including MHC-I, for degradation. We reasoned that RIPK2 might modulate NBR1-mediated autophagy–lysosomal degradation of MHC-I. To test this hypothesis, we first applied immunoprecipitation assays to detect whether RIPK2 is within the same protein complex that contains MHC-I and NBR1. We noticed the physical interaction of RIPK2 with HLA-A (Fig. 5F; Supplementary Fig. S7K) and with NBR1 (Fig. 5G; Supplementary Fig. S7L) in human PANC-1 cells. In line with a previous report (8), knocking down *NBR1* resulted in an increase in MHC-I total protein levels and fully rescued MHC-I expression in PANC-1 cells with ectopical RIPK2 overexpression (Fig. 5H-J). Furthermore, immunofluorescence revealed that *RIPK2* knockdown led to less frequent colocalization between NBR1 and MHC-I in human PDAC cells (Fig. 5K; Supplementary Fig. S7M). Collectively, these data suggest a crucial role for RIPK2 in the regulation of MHC-I levels through NBR1-mediated autophagy–lysosomal degradation.

RIPK2 Ubiquitination Promotes NBR1-mediated MHC-I Degradation

RIPK2 has an N-terminal kinase domain (KD) and a C-terminal caspase activation and recruitment domain (CARD). To investigate how RIPK2 may act to regulate NBR1-mediated MHC-I degradation, we generated a series of mutants that lack the CARD domain or known phosphorylation (D146) and ubiquitination (K410/538) sites. Immunoprecipitation assays revealed that the functional interaction of RIPK2 with HLA-A and NBR1 requires the ubiquitination of RIPK2. Specifically, the K410/538R mutant almost entirely lost its interaction with HLA-A and NBR1, whereas the ΔCARD and D146N mutants partially retained their binding activity (Fig. 6A; Supplementary Fig. S8A). Previous studies have shown that RIPK2 ubiquitination of RIPK2 by several ubiquitin E3 ligases, including x-chromosome-linked inhibitor of apoptosis (XIAP), is critical for NOD2-mediated signaling and subsequent NF-κB and MAPK activation (34, 35). We then evaluated the levels of RIPK2 ubiquitination in human PDAC and normal cells. Interestingly, we detected substantially higher levels of ubiquitinated RIPK2 in PDAC cells than in pancreatic ductal epithelial cells (Fig. 6B). In addition, ectopic expression of K410/538R mutant in shRIPK2-expressing PANC-1 cells resulted in significantly reduced RIPK2 ubiquitination as compared with wild-type RIPK2 control (Fig. 6C). Similar results were observed by ectopic expression of murine K537R mutant (corresponding to human K410/583R) in shRipk2-expressing KPC^{mut} cells

Figure 5. RIPK2 promotes MHC-I trafficking to lysosomes via NBR1. **A** and **B,** Left, Western blot analyses of class I HLA expression in shRIPK2 or shNT-expressing PANC-1 cells treated with cycloheximide (CHX, **A**) or bafilomycin A1 (BafA1, **B**). Right, quantitative estimates of class I HLA levels based on Western blot analyses. Mean ± SD, *n* = 3 biological replicates. **C** and **D,** Effect of *RIPK2* depletion on lysosomal localization of class I HLA in tumor cells. shRIPK2/shNT PANC-1 cells with or without GFP-LC3 expression were stained for LAMP1 or class I HLA. Cell nucleus (blue) was stained with 4′,6-diamidino-2-phenylindole (DAPI). Representative immunofluorescence images and quantification of class I HLA colocalization with LAMP1 or LC3 are shown. Scale bars, 5 μm. *n* = 3 biological replicates (10 fields). **E,** Western blot analysis of LC3B (LC3-I and -II) level in PANC-1 cells upon treatment with or without BafA1 (100 nmol/L, 24 hours). *n* = 3 biological replicates. Representative images are shown. **F** and **G,** RIPK2 is physically associated with HLA-A or NBR1. PANC-1 cells expressing Myc-tagged RIPK2 and Flag-tagged HLA-A or NBR1 were analyzed by co-IP and Western blot using indicated antibodies. **H** and **I,** Western blot analysis of class I HLA expression levels in RIPK2-overexpressing BxPC3 (**H**) or MIA Paca-2 (**I**) cells with or without NBR1 depletion. Mean ± SD, *n* = 3 biological replicates, two-tailed *t* test. **J,** Class I HLA expression levels were determined by flow cytometry in RIPK2-overexpressing MIA Paca-2 cells with or without NBR1 depletion. Mean ± SD, *n* = 3 biological replicates, two-tailed *t* test. **K,** Effect of *RIPK2* knockdown on the colocalization of class I HLA with NBR1. shRIPK2 or shNT PANC-1 cells expressing NBR1-GFP were stained for class I HLA (red). Cell nucleus (blue) was stained with DAPI. Representative immunofluorescence images and quantification of class I HLA colocalization with NBR1 are shown. Scale bars, 5 μm. *n* = 3 biological replicates (10 fields).

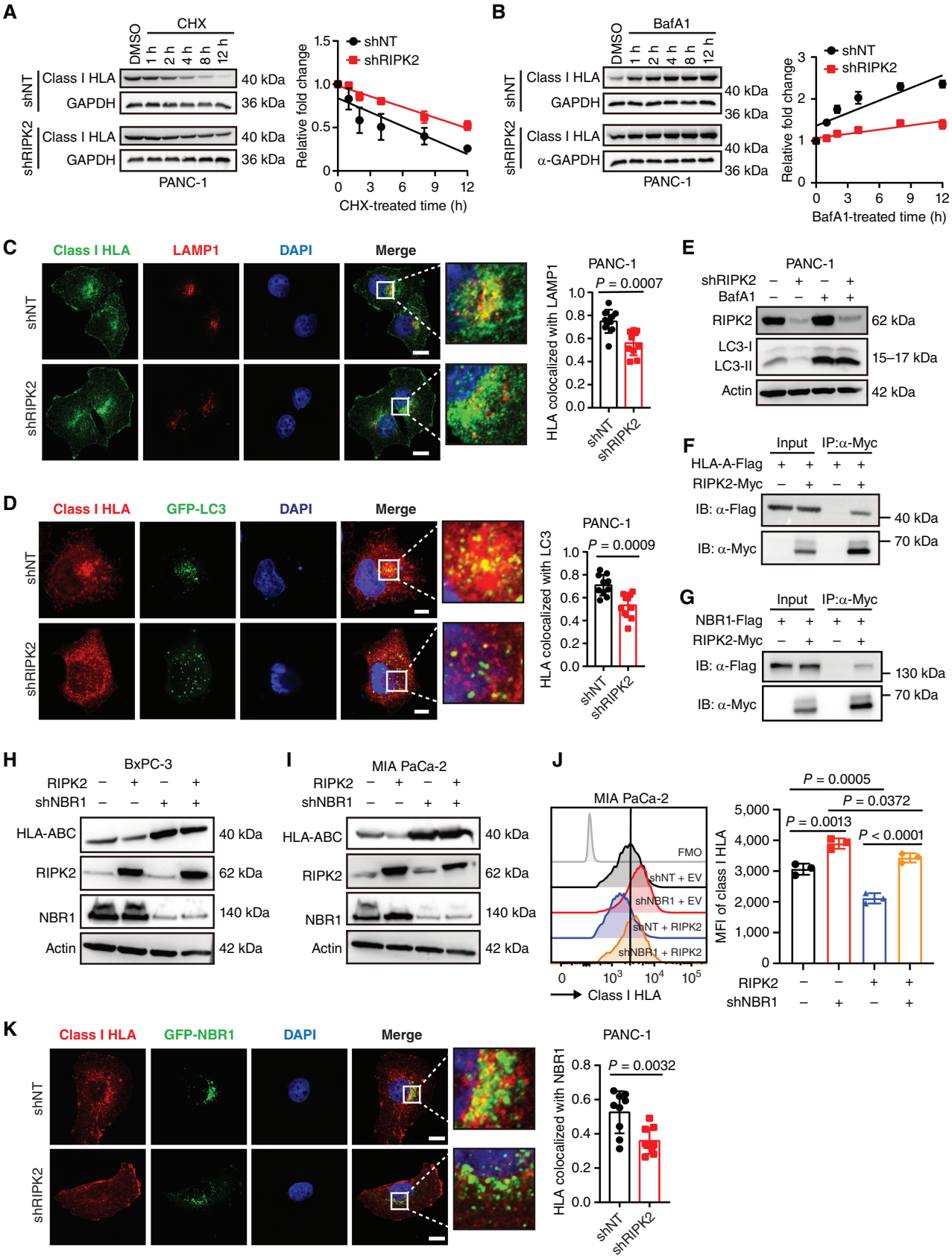

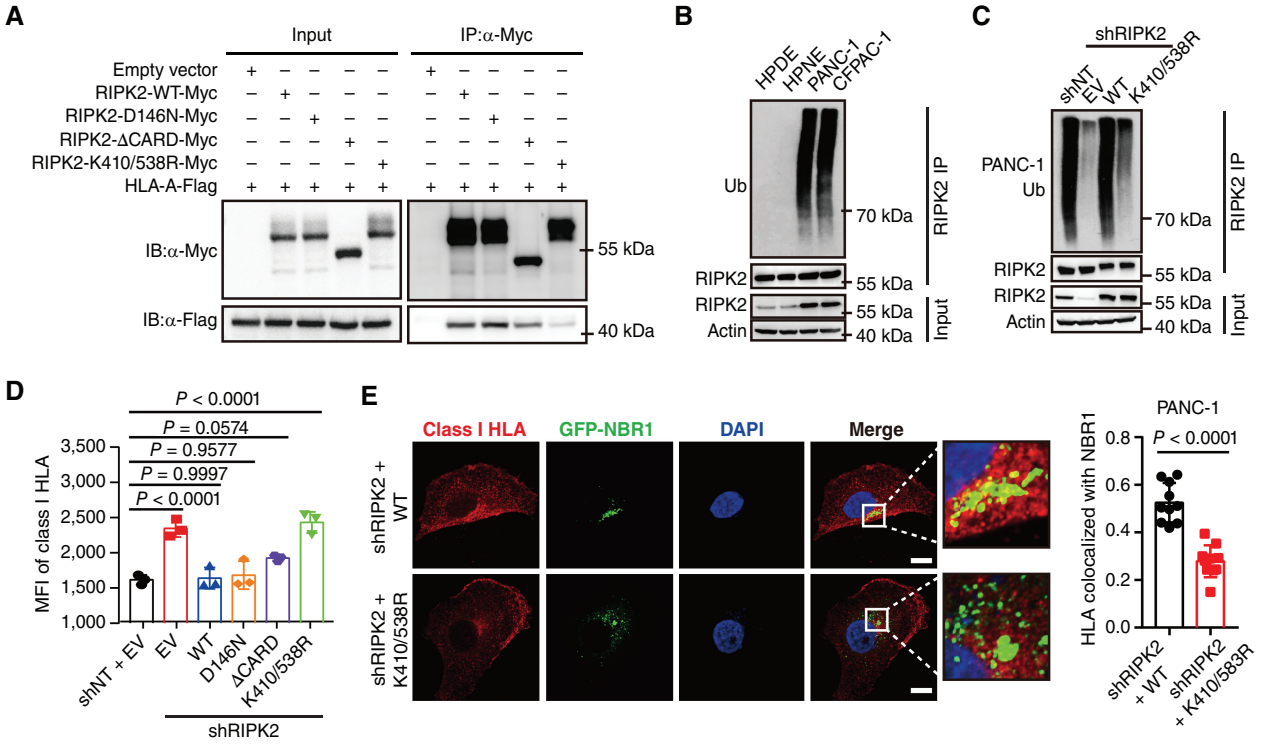

Figure 6. RIPK2 ubiquitination promotes NBR1-mediated MHC-I degradation. **A,** Ubiquitination of RIPK2 is essential for its interaction with HLA-A. Flag-tagged HLA-A and Myc-tagged wild-type (WT) or mutant RIPK2 were overexpressed in 293T cells. RIPK2 was immunoprecipitated and blotted with indicated antibodies. $n = 3$ biological replicates. **B,** Western blot analysis of RIPK2 immunoprecipitates with indicated antibodies in HPDE, HPNE, PANC-1, and CFPAC-1 cells. RIPK2 was immunoprecipitated, and poly-ubiquitin was detected using an anti-ubiquitin antibody. **C,** Western blot analysis of RIPK2 immunoprecipitates in PANC-1 cells with indicated antibodies. Wild-type (WT) or K410/538R mutants were ectopically overexpressed in shRIPK2-expressing PANC-1 cells. RIPK2 was immunoprecipitated, and poly-ubiquitin was detected using an anti-ubiquitin antibody. **D,** Effect of RIPK2 ubiquitination on class I HLA expression on plasma membrane. Wild-type or mutant RIPK2 were transduced into shRIPK2 PANC-1 cells, and surface class I HLA levels were analyzed by flow cytometry. Mean ± SD, $n = 3$ per group, two-tailed t test. **E,** Effect of K410/538R mutant on the colocalization of class I HLA with NBR1. Wild-type or mutant RIPK2 were transduced into shRIPK2 PANC-1 cells expressing NBR1-GFP and were stained for class I HLA (red). Cell nucleus (blue) was stained with DAPI. Representative immunofluorescence images and quantification of class I HLA colocalization with NBR1 are shown. Scale bar, 5 μm. $n = 3$ biological replicates (10 fields). (*continued on following page*)

(Supplementary Fig. S8B). In contrast to its role in innate immunity, RIPK2 depletion only had a marginal effect on the activation of canonical NF-κB and MAPK signaling pathways in human PDAC cells (Supplementary Fig. S8C and S8D).

To examine the functional consequence of these mutants, we introduced each of them into RIPK2-depleted PDAC cells and compared MHC-I levels on the plasma membrane with wild-type cells. Ectopic expression of the K410/538R mutant in human PDAC cells expressing shRIPK2 had no significant effect on the presentation of MHC-I on cell surface, whereas partially binding-deficient forms of RIPK2 reduced MHC-I presentation (Fig. 6D; Supplementary Fig. S8E). Using immunofluorescence, we found that overexpression of the K410/538R mutant was unable to rescue the colocalization of MHC-I with NBR1 in RIPK2-depleted human PDAC cells compared with wild-type control (Fig. 6E; Supplementary Fig. S8F). Moreover, treatment with GSK583 (a preclinical RIPK2-selective inhibitor, RIPK2i) or ponatinib (an FDA-approved multitarget inhibitor) efficiently abolished RIPK2 ubiquitination in both human and mouse PDAC cells (Fig. 6F; Supplementary Fig. S8G). Consequently, pharmacologic inhibition of RIPK2 using GSK583 or ponatinib substantially increased the presentation of MHC-I on multiple PDAC cell surfaces (Fig. 6G and H; Supplementary Fig. S8H–S8K). To further test the effect of RIPK2 ubiquitination on the antitumor immune response *in vivo*, shRipk2 KPC^{mut} cells expressing wild-type or K537R mutant were subcutaneously transplanted into C57BL/6 mice. *Ripk2* knockdown resulted in a significant reduction in tumor burden, which was fully reversed by wild-type RIPK2, but only partially rescued by the K537R mutant (Fig. 6I and J; Supplementary Fig. S8L). Furthermore, tumors that carried the K537R mutant exhibited significantly higher MHC-I expression than wild-type tumors, whereas CD8$^+$ T-cell infiltration was only slightly increased (Fig. 6K and L). Taken together, these results indicate that RIPK2 ubiquitination in K410/538 is critical for NBR1-mediated degradation of MHC-I.

RIPK2 Ablation Potentiates the Efficacy of PD-1 Blockade

Despite the reinvigorated antitumor immune response after RIPK2 ablation, the expression level of the PD1 checkpoint in CD8$^+$ T cells remains robust (Supplementary Fig. S5D). Therefore, we hypothesized that a combination of RIPK2 targeting and ICB could further block tumor progression. Thus, mice bearing orthotopic shNT or shRipk2 KPC^{mut} tumors

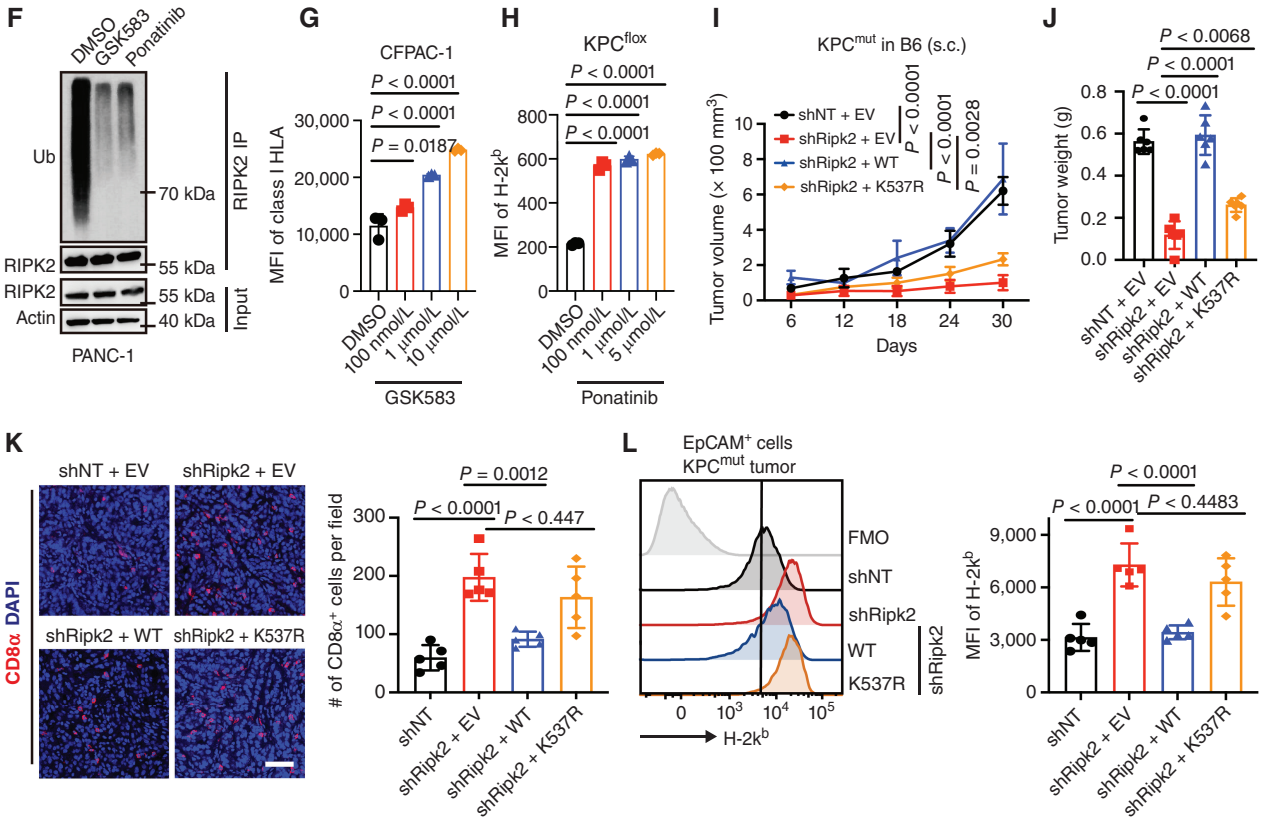

Figure 6. ***(Continued)*** **F,** Western blot analysis of RIPK2 immunoprecipitates in PANC-1 cells with indicated antibodies. Cells were treated with GSK583 (10 μmol/L), ponatinib (5 μmol/L), or DMSO for 48 hours. RIPK2 was immunoprecipitated, and poly-ubiquitin was detected using an anti-ubiquitin antibody. Effect of RIPK2 inhibitors on MHC-I expression on plasma membrane. PANC-1 (**G**) or KPC^{mut} (**H**) cells were treated with GSK583 (10 μmol/L), ponatinib (5 μmol/L), or DMSO for 48 hours, and surface MHC-I levels were analyzed by flow cytometry. Mean ± SD, $n = 3$ per group, two-tailed t test. **I–K,** Effect of murine K537R mutant on subcutaneously implanted KPC^{mut} tumor growth in wild-type C57BL/6 mice. Tumor volume (**I**), weight (**J**), and quantification and representative image of tumor-infiltrating CD8$^+$ T cells (**K**) are shown. Mean ± SD, $n = 5$–6 per group. Two-way ANOVA (**I**) and two-tailed t test (**J** and **K**). Scale bar, 50 μm. **L,** H-2K^b expression levels in EpCAM$^+$ KPC^{mut} tumor cells were determined by flow cytometry. shRipk2 KPC^{mut} cells transduced with wild-type or murine K537R mutant were orthotopically implanted into C57BL/6 mice, and tumors were harvested on days 21–25 after inoculation. Mean ± SD, $n = 5$ per group, two-tailed t test.

were randomized and treated with α-PD-1 or IgG control. As expected, knockdown of *Ripk2* alone markedly reduced tumor growth and increased life expectancy compared with that observed in the control group (Fig. 7A and B), leading to approximately 50% remission (6 of 11 mice). In line with previous reports, α-PD-1 therapy alone had no effect on tumor progression in our model, suggesting intrinsic resistance to immunotherapy. However, combining *Ripk2* knockdown with α-PD-1 dramatically boosted overall survival, leading to a 90.9% (10 of 11 mice) complete regression (Fig. 7A and B). These mice survived without signs of residual tumors or liver metastases on day 120, although treatments were stopped on day 80 (Fig. 7C; Supplementary Fig. S9A and S9B). Similar results were observed when using the KPC^{flox} syngeneic mouse model, recapitulating the poor immunogenicity and rapid progression of human PDAC. α-PD-1 failed to eradicate any tumors, while *Ripk2* knockdown led to approximately 50% remission (3 of 5 mice). Strikingly, the combination of α-PD-1 and *Ripk2* knockdown eliminated all KPC^{flox} tumors (7 of 7 mice; Fig. 7D and E).

To investigate whether pharmacologic inhibition of RIPK2 could improve PDAC immunotherapy, mice bearing KPC^{mut} tumors were randomized into four groups, followed by daily treatment with vehicle control or ponatinib (20 mg/kg/day). Compared with single-agent treatments or vehicle-treated control, α-PD-1 plus ponatinib significantly inhibited tumor burden and increased overall survival, although the combined effects were less pronounced than *RIPK2* genetic depletion (Fig. 7F and G; Supplementary Fig. S9C). The median survival benefit by adding α-PD-1 to the combination was 13 days compared with ponatinib alone and 25 days compared with vehicle control, representing an almost two-fold increase in the median survival time (Fig. 7F). This improvement in immunotherapeutic efficacy was associated with a significantly disrupted desmoplastic TME, reduced liver metastasis, and increased numbers of CD8$^+$ CTLs, which are in proximity to target pan-cytokeratin$^+$ PDAC cells (Fig. 7H; Supplementary Fig. S9D and S9E). Notably, the combined treatment had no notable toxicity *in vivo*, as reflected by negligible body weight changes (Supplementary Fig. S9F). Similarly, mice carrying KPC^{mut} tumors were treated with α-PD-1 plus GSK583 (10 mg/kg/day), a preclinical RIPK2-selective inhibitor, which showed a significant extension of overall survival and reduction of tumor burden (Fig. 7I and J; Supplementary Fig. S9G).

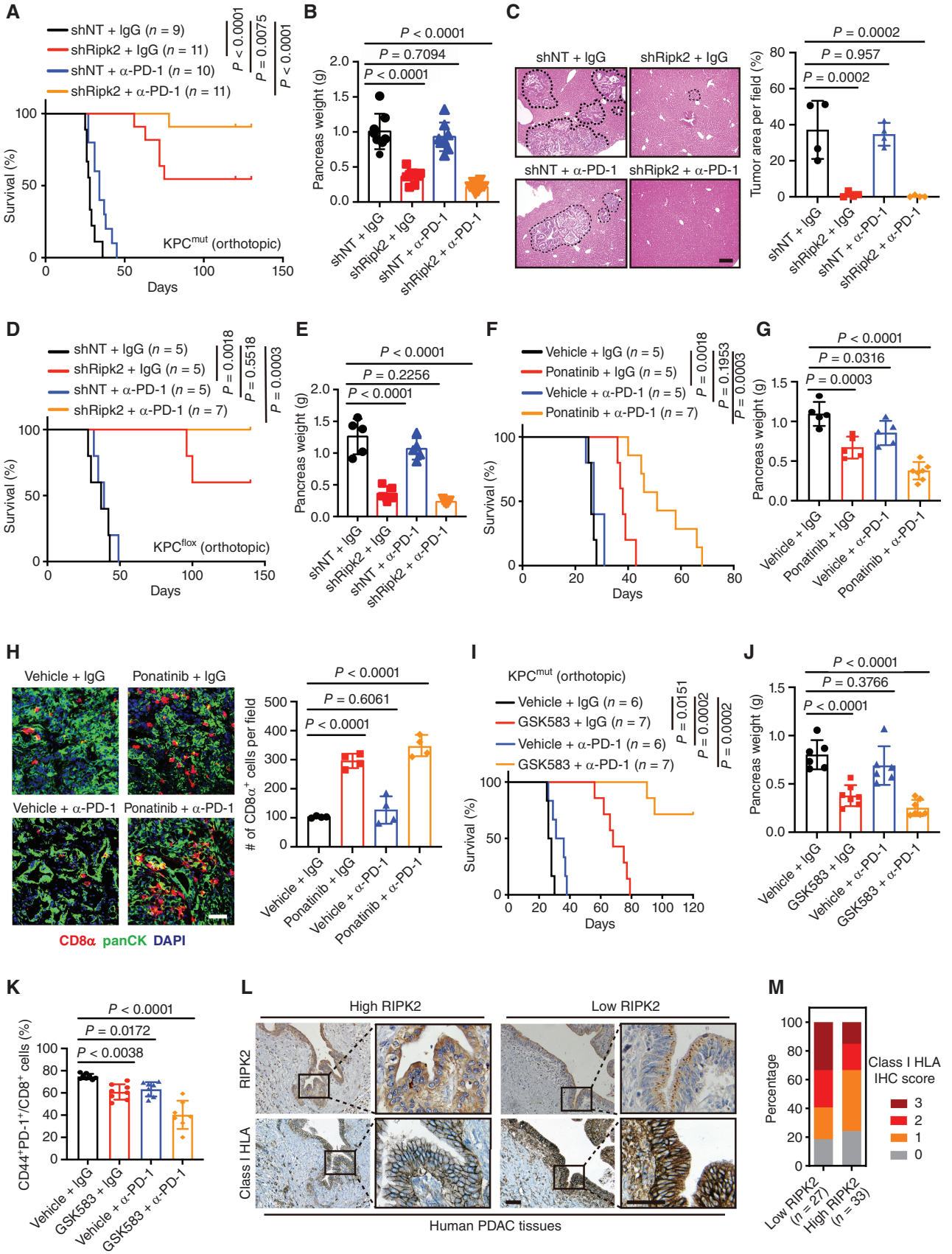

Consistent with this enhanced survival, the combination of α-PD-1 with GSK583 promoted a synergistic expansion of total CD8$^+$ T cells and granzyme B$^+$ CD8 T cells within the PDAC TME (Supplementary Fig. S9H–S9K). Moreover, α-PD-1 plus GSK583 treatment induced pan T-cell activation, marked by a reduction in terminally exhausted CD8$^+$ T cells (CD44$^+$PD1$^+$) and an expansion of stem-like memory cells (TCF1/7$^+$), which are considered the "recoverable" fraction of exhausted CD8$^+$ T cells (ref. 36; Fig. 7K; Supplementary Fig. S9L). Combined therapy has not shown significant toxicity *in vivo*, as evidenced by the absence of substantial changes in body weight (Supplementary Fig. S9I). To further study the clinical relevance of our findings, we evaluated the expression of the RIPK2 and MHC-I proteins with continued series of human PDAC tissue sections. IHC analysis revealed that aberrant RIPK2 expression was negatively correlated with that of MHC-I (Fig. 7L and M). Together, these results indicate that genetic or pharmaceutical inhibition of RIPK2 in combination with α-PD-1 strongly blunts tumor progression, paving the way toward a potential therapeutic strategy for immunologically "cold" PDAC tumors.

DISCUSSION

Pancreatic cancer remains one of the most lethal malignancies because of its aggressive nature and lack of effective treatment options (1, 2). Almost all multidrug chemotherapies and even the most recent ICB therapy have failed to offer PDAC patients a promising treatment solution (5, 37), highlighting the urgent need to identify novel therapeutic targets. CRISPR/Cas9 has expanded the use of functional genetic screens to rapidly discover targets in antitumor immunity (38). Compared with *in vitro* screenings or heterotopic skin tumor models, orthotopic syngeneic models are the most physiologically relevant systems for screening for novel immune modulators. Using small, focused libraries is a practical strategy for *in vivo* CRISPR screens, and we performed kinome- and membranome-centered *in vivo* CRISPR screens in orthotopic PDAC models to discover targets that could sensitize PDAC to antitumor immunity in host mice that differ in microenvironmental competence. These targets can be quickly translated into clinical applications and benefit a significant subset of patients with PDAC. To our knowledge, this is the first reported screening to identify immune modulators within endogenous pancreatic TME systematically. We found that RIPK2 is a crucial driver of immune evasion and that genetic or pharmacologic targeting of *RIPK2* in tumor cells sensitizes PDAC to ICB therapy, leading to complete or partial regression and prolonged survival. Interestingly, multiple known mediators of immune evasion (e.g., *Ptpn2* and *Ripk1*) were also identified as the top candidates (20, 39), validating the robustness of our screens.

RIPK2 is a downstream adaptor kinase for the NOD1/2 signaling pathway, mediating subsequent NF-κB and MAPK activation (40). Over the last decade, RIPK2 has been well characterized in the regulation of inflammation and innate immune signaling (24). Emerging evidence suggests that RIPK2 kinase activity may also modulate tumorigenesis. Several studies have reported aberrant expression of RIPK2 in various cancers, including prostate, gastric, lung, and kidney (41–44). However, little is known about the role of RIPK2 in antitumor immunity. Here, our data suggest that RIPK2 is an immune regulatory molecule in the context of PDAC tumor immunity. This antitumor response is primarily attributed to the host adaptive immune response, particularly the boosted tumor-infiltrating CD8$^+$ CTLs. Mechanistically, targeting RIPK2 not only abolishes the ability of CAFs to promote desmoplastic TME but also promotes T-cell activation and effector states through impairing NBR1-mediated autophagy-lysosomal MHC-I degradation. Interestingly, RIPK1, the "founding member" of the RIPK family, was recently shown to be a master regulator of immune tolerance in PDAC and confers cell-extrinsic and -intrinsic resistance to ICB therapy (39, 45).

MHC-I plays a critical role in the adaptive immune system by presenting antigens derived from intracellular proteins to CD8$^+$ CTLs (46, 47). Loss of MHC-I expression is a well-documented strategy utilized by cancer cells to evade elimination by the immune system (48–50). MHC-I expression is downregulated in human and mouse PDAC tumors (51, 52). However, unlike other types of cancer, MHC-I mutations are rare in human PDAC, suggesting that other mechanisms may be responsible for the loss of MHC-I (53, 54). We provide evidence that RIPK2 is a driver of autophagy-dependent degradation of MHC-I and subsequent immune evasion, which echoes previous studies showing that MHC-I is actively degraded through an autophagy-dependent mechanism (8, 55). RIPK2 has been shown to be critical for NOD1/2-induced autophagy and inflammatory responses (56–58), although the detailed mechanisms still need to be fully understood. Previous studies reported that antibacterial autophagy stimulation is dependent on autophagy-related protein 16–1 (ATG16L1) and the ubiquitin ligase XIAP (34, 58). Another study showed that RIPK2 regulates antivirus autophagy in a

Figure 7. RIPK2 ablation potentiates the efficacy of PD-1 blockade. **A,** Survival curve of orthotopically implanted shNT and shRipk2 KPC^{mut} tumor-bearing mice treated with anti–PD-1 or IgG control (shNT + IgG $n = 9$, shRipk2 + IgG $n = 11$, shNT + α-PD1 $n = 10$, shRipk2 + α-PD1 $n = 11$). Pool of two independent experiments. Log-rank Mantel–Cox test. Pancreas weight (**B**, $n = 9$–11 per group) and liver metastasis (**C**, $n = 4$ per group) of orthotopically implanted shNT and shRipk2 KPC^{mut} tumor-bearing mice treated with anti–PD-1 or IgG control. Mean ± SD, two-tailed *t* test. Scale bar, 100 μm. **D,** Survival curve of orthotopically implanted shNT and shRipk2 KPC^{flox} tumor-bearing mice treated with anti–PD-1 or IgG control (shNT + IgG $n = 5$, shRipk2 + IgG $n = 5$, shNT + α-PD1 $n = 5$, shRipk2 + α-PD1 $n = 7$). Log-rank Mantel–Cox test. **E,** Pancreas weight of orthotopically implanted shNT and shRipk2 KPC^{flox} tumor-bearing mice treated with anti–PD-1 or IgG control. Mean ± SD, $n = 5$–7 per group, two-tailed *t* test. Survival curve (**F**, $n = 5$–7 per group), end-stage pancreas weight (**G**, $n = 5$–7 per group), and quantification of tumor-infiltrating CD8$^+$ T cells (**H**, $n = 4$ per group) of orthotopically implanted KPC^{mut} tumor-bearing mice treated with ponatinib and/or anti–PD-1. Log-rank Mantel–Cox test (**F**) and two-tailed t-test (**G** and **H**). Scale bar, 50 μm. Survival curve (**I**), and end-stage pancreas weight (**J**) of orthotopically implanted KPC^{mut} tumor-bearing mice treated with GSK583 and/or anti–PD-1 (vehicle + IgG $n = 6$, GSK583 + IgG $n = 7$, vehicle + α-PD1 $n = 6$, GSK583 + α-PD1 $n = 7$). Log-rank Mantel-Cox test (**I**) and two-tailed t-test (**J**). **K,** Mice bearing KPC^{mut} tumors were treated as in **I**, and intratumoral immune cells were analyzed by flow cytometry for CD44 and PD-1 as a fraction of CD8$^+$ T cells. Mean ± SD, $n = 7$–8 per group. Two-tailed *t* test. **L** and **M,** Representative RIPK2 and class I HLA IHC staining in human PDAC tissues (**L**). Class I HLA expression between patients with low ($n = 27$) and high ($n = 33$) expression levels of RIPK2 was compared (**M**).

kinase-dependent manner by phosphorylating the mitophagy inducer UNC-51-like kinase (ULK1; ref. 56). Consistent with these important discoveries, our work is a novel expansion in this active research area, suggesting that aberrant expression of RIPK2 dampens MHC-I levels in PDAC cells through NBR1-mediated autophagy-lysosomal degradation. Notably, the interaction between RIPK2 and NBR1 mainly depends on the K410/538 ubiquitination sites but only partially relies on the CARD domain. This result agrees with the previous study that showed the role of RIPK2 ubiquitylation in promoting inflammation and tumor neutrophil infiltration in melanoma (59).

Interestingly, we observed that pharmacologic inhibition of RIPK2 with ponatinib or GSK583 inhibitors did not robustly abrogate tumor progression in orthotopic PDAC models, compared with genetic depletion by knockdown or knockout. This discrepancy may be partially explained by the unfavorable pharmacodynamic efficacy of RIPK2i *in vivo* or the contribution of other RIPK2 domains except for the K410/538 ubiquitination sites (60). Indeed, RIPK2 depletion led to a marked reduction in tumor burden, which was fully reversed by wild-type RIPK2, as expected. However, this reduction was also partially rescued by the K537R mutant. Moreover, knocking down *Ripk2* in shH2k1 KPC^{mut} tumor cells still significantly reduced tumor growth, although the effect is less pronounced than in shNT control cells. These results indicate that other domains of RIPK2 may also play essential roles in driving an MHC-I-independent immunosuppressive program to enable tumor progression, highlighting the need to develop more potent inhibitors. Notably, because *Ripk2* is dispensable for mouse embryo development (61), the targeted degradation of RIPK2 could be more promising than traditional small-molecule inhibitors. Recently, proteolysis targeting chimeras (PROTAC) targeting RIPK2 with attractive pharmacokinetic profiles have been developed, offering a promising alternative strategy for RIPK2 blockade (60, 62).

This study focused on the adaptive immune response, particularly the boosted tumor-infiltrating CD8$^+$ CTLs. However, we could not exclude the possibility that other immune populations, such as dendric cells (DC), natural killer cells (NK), macrophages, and neutrophils, may also play an essential role in the antitumor immune response in *RIPK2*-deficient tumors. Our scRNA sequencing and flow cytometry analyses of intratumoral immune cell populations revealed increased DCs, NKs, and proinflammatory TAMs but decreased anti-inflammatory TAMs. DCs play an essential role in antigen presentation and T-cell priming (63), whereas reprogramming TAMs toward a proinflammatory phenotype supports enhanced antitumor immune responses. These results indicate that the enhanced antitumor immune response in RIPK2-deficient tumors may involve multiple innate immune populations. The other domains of RIPK2 may also drive various immune cells to enable tumor progression. Investigating how these changes are mediated in innate immune cells and what roles different domains of RIPK2 play will be essential subjects of future work.

In summary, we performed an *in vivo* CRISPR screening and identified RIPK2 as a critical driver of immune evasion and a promising candidate to sensitize PDAC immunotherapy. Targeting RIPK2 with genetic depletion or small-molecule inhibitors sensitizes PDAC to ICB therapy, leading to complete or partial regression and prolonged survival. Functional and mechanistic studies showed that tumor-intrinsic RIPK2 ablation disrupts desmoplastic TME and restores surface levels of MHC-I through eliminating NBR1-mediated autophagy–lysosomal degradation (Supplementary Fig. S10). Thus, combining RIPK2 inhibition with ICB therapy, such as anti–PD-1 treatment, could be a potential novel immunotherapy strategy for patients with PDAC.

METHODS

Reagents

Detailed information on all reagents used in this article is listed in Supplementary Table S3.

Cell Culture

The cell lines PANC-1, CFPAC-1, MIA Paca-2, BxPC-3, Hs766T, AsPC-1, HPAC, and hTERT-HPNE were obtained from the ATCC and cultured under standard conditions specified by the manufacturer. The mouse pancreatic cancer cell lines UN-KC-6141 (26), HPDE. AK14837/838, KPC^{mut,} and KPC^{flox} were provided by Dr. Surinder K. Batra (University of Nebraska) and Dr. Haoqiang Ying and Dr. Cassian Yee (MD Anderson Cancer Center, Houston, TX). Cell lines were maintained in a humidified atmosphere containing 5% CO_2 at 37°C and were regularly tested and verified to be *Mycoplasma* negative using Mycoplasma Detection Kit (Thermo Fisher Scientific) or via conventional PCR. All cell lines were banked in multiple aliquots on receipt to reduce the risk of phenotypic drift.

Expression Constructs

The cDNA clones expressing human RIPK2 (#O0073) and mouse RIPK2 (#Mm13952) were obtained from GeneCopoeia. Plasmid expressing HLA-A (#100154) was obtained from Addgene. GFP-NBR1 was a gift from QM Sun (Zhejiang University, Zhejiang, China). Flag- or Myc-tagged expressing constructs were generated by subcloning the cDNA of RIPK2, HLA-A, and NBR1 to pCDH-puro or pHS-AVC lentiviral vector. Human or mouse RIPK2 kinase, ubiquitination, or CARD domain truncation mutants were generated from site-specific mutagenesis of RIPK2 (Vazyme) or via overlapping PCR. Plasmids were sequenced to confirm the mutations. Plasmids were purified by the SANGON Miniprep Kit or NucleoBond Xtra Midi kit (MACHEREY-NAGEL). Specific primers are included in Supplementary Table S4.

Mouse Strains and Tumor Models

Nude mice (C57BL/6J$^{nu/nu}$, 6–8 weeks) and wild-type C57BL/6J (6–8 weeks) were purchased from the Shanghai Laboratory Animals Center. The KTC (*Ptf1a-Cre;LSL-Kras*$^{G12D/+}$*;Tgfbr2*$^{flox/flox}$) (28) and KPC^{flox} (*Pdx1-Cre;LSL-Kras*$^{G12D/+}$*;Trp53*$^{flox/flox}$; refs. 26, 27) genetically engineered mouse model were described previously. OT-I C57BL/6-Tg(TcraTcrb)1100Mjb/J mice were purchased from the Jackson laboratory. All mice were bred and maintained in the animal facility of the Zhejiang University School of Medicine. All studies were approved and supervised by the Animal Care and Use Committee of the Zhejiang University School of Medicine (#24817).

In Vivo *CRISPR Screening*

In vivo CRISPR screen was performed as described previously (19, 64). Briefly, after transduction of KPC^{mut} cells with lentivirus, single clones were isolated, and doxycycline-induced Cas9 expression was confirmed by Western blot analysis. The Cas9-mediated DNA-editing

efficiency was further confirmed with sgRNAs targeting the *PD-L1* gene. KPC^{mut}-Cas9 clones with validated Cas9 expression were transduced with sgRNA libraries targeting 2,012 kinase genes and 954 membrane genes (ref. 23; 10 gRNAs per gene) at a MOI of 0.2 with at least 200-fold coverage (cells per construct). After selection with puromycin, KPC^{mut} cells transduced libraries were either expanded *in vitro* or orthotopically implanted into nude mice (immunodeficient) and C57BL/6 mice (immunocompetent). Mice were euthanized on day 21 after implantation, and tumor genomic DNA was extracted from the whole tumor tissue using the Qiagen DNA blood Midi kit. Nested PCR was used to amplify the sgRNA region, and NGS was performed on Illumina HiSeq to determine sgRNA abundance. After trimming adaptor sequences using Cutadapt, gRNAs were mapped and normalized, and the significantly enriched or depleted sgRNAs from any comparison of conditions were identified by the MAGeCK algorithm (65).

Genetic Knockdown and CRISPR Knockout

The shRNAs targeting the human *RIPK2* gene or mouse *Ripk2* and *H2k1* genes were cloned into pLKO.1-puro or Tet-pLKO-puro lentiviral vectors. To generate lentivirus, HEK-293T cells were co-transfected with shRNA expression plasmids targeting *Ripk2* or scramble sequences and packaging plasmids psPAX2 and pMD2.G using PEI Transfection Reagents. Human and mouse PDAC cells were then transduced by culturing with viral supernatants in the presence of polybrene (Solarbio) and then selected with puromycin or blasticidin. Single colonies with robust knockdown efficiencies (>70%) were chosen for the downstream experiments.

Knockout cells were generated with lentivirus-mediated CRISPR-Cas9 technology. sgRNAs specific for the mouse *Ripk2* gene were designed using an online CRISPR design tool (F. Zhang lab, MIT, Boston, MA). sgRNA sequences targeting the *Ripk2* gene were cloned into plentiCRISPR-v2 using the standard protocol. To generate the knockout cell lines, KPC^{mut} cells were infected with sgRNA-encoding lentivirus and then selected with puromycin for 3 days. Living cells were seeded in 96-well plates following limiting dilution protocol, and then the clones emerging from the plates were expanded, and expression of the target protein was validated by Western blotting. Specific primers are included in Supplementary Table S4.

Quantitative RT-PCR

Cells were lysed with RNAiso Plus reagent (Takara), and total RNA was isolated according to the manufacturer's instructions. An equal amount of total RNA was then reverse transcribed (RT) using an iScript cDNA synthesis kit (Bio-Rad). The resulting cDNA was used for quantitative PCR using iTaq Universal SYBR Green Supermix qPCR kit (Bio-Rad) with gene-specific primers. The results were normalized with β-actin as internal control. Specific primers are included in Supplementary Table S4.

Immunoblotting

Cultured cells were prewashed with PBS and lysed on ice with RIPA buffer (50 mmol/L Tris, pH 7.4, 150 mmol/L NaCl, 1% Nonidet P-40, 0.5% sodium deoxycholate, and 0.1% SDS) supplemented with protease inhibitor Cocktail (Roche) and phosphatase inhibitor mixture (Thermo Fisher Scientific). Cell lysates were clarified by centrifugation at 13,000 × *g* at 4°C for 10 minutes, and the protein concentration was determined by a BCA kit (Thermo Fisher Scientific). Equal amounts of protein lysates were resolved by SDS-PAGE and transferred to the polyvinylidene difluoride membrane after blocking with 5% nonfat milk. The membrane was incubated overnight with indicated primary antibodies at 4°C and then horseradish peroxidase–conjugated secondary antibodies at room temperature for 1 hour. Finally, the relevant protein was visualized by SuperSignal West Pico Plus Chemiluminescent Substrate (Thermo Fisher Scientific) according to the manufacturer's instructions. The results shown for each blot represent at least three independent experiments. Detailed information on antibodies is listed in Supplementary Table S3.

Immunoprecipitation and Ubiquitination Assay

For immunoprecipitation, whole-cell lysates were prepared by incubating cell pellets in NP40 lysis buffer (0.5% NP-40, 20 mmol/L Tris, pH 7.4, 150 mmol/L NaCl, 2 mmol/L EDTA, 10% glycerol, and 1 mmol/L phenylmethylsulfonylfluoride) supplemented with protease inhibitor Cocktail (Roche) on ice for 30 minutes. After centrifugation at 13,000 × *g* at 4°C for 10 minutes, equal amounts of cell lysates were immunoprecipitated with 0.5 μg of indicated antibodies at 4°C overnight and then incubated with protein A/G magnetic beads (Bimake) at 4°C for 1 hour. The protein-captured beads were washed three times with lysis buffer and eluted with SDS loading buffer. The eluted protein or protein complexes were separated on SDS-PAGE gel and analyzed by immunoblotting. Detailed information on antibodies is listed in Supplementary Table S3.

Immunoprecipitation of endogenous ubiquitylated RIPK2 was carried out as described previously (59). Forty-eight hours after transfection or inhibitor treatment, cells were treated with 5 μmol/L MG132 (Sigma) for 12 hours. Cells were then harvested and resuspended in NP40 lysis buffer in addition to N-ethylmaleimide (Sigma-Aldrich) and protease inhibitor cocktail (Roche) on ice for 30 minutes. After centrifugation, lysates were immunoprecipitated with 2 μg of RIPK2 antibody at 4°C overnight and then incubated with protein A/G magnetic beads (Bimake) at 4°C for 1 hour. The immunoprecipitates were washed with lysis buffer and then immunoblotted with indicated antibodies. Detailed information on antibodies is listed in Supplementary Table S3.

Mass Spectrometry

To identify RIPK2-interacting proteins, PANC-1 cells overexpressing Myc-tagged RIPK2 were lysed by incubating cell pellets in NP40 lysis buffer. Cell lysates were immunoprecipitated with anti-Myc tag antibodies at 4°C overnight and then incubated with protein A/G magnetic beads (Bimake) at 4°C for 1 hour. The immunoprecipitates were resolved using SDS-PAGE, extracted from the gel, and subjected to LC/MS-MS sequencing by Applied Protein Technology Co., Ltd. The resulting MS-MS data were blasted against the human FASTA from UniProt. Data analysis was performed with Maxquant software. Peptides that were exclusively assigned to a given protein group were considered unique.

Immunofluorescence Staining

Immunofluorescence staining and imaging were performed as previously described (66). For mouse PDAC tumors, 5-μm–thick frozen sections were washed with PBST, blocked with blocking buffer (5% goat serum in PBST) for 1 hour at room temperature, and stained with primary antibodies at 4°C overnight. For plasma membrane colocalization experiments, human PDAC cell lines were seeded on coverslips coated with poly-lysine overnight. After washing with Hanks balanced salt solution (HBSS), cells were stained with Alexa Fluor 594–conjugated wheat germ agglutinin (WGA) at 37°C for 10 minutes before fixation and then incubated with primary antibodies at 4°C overnight without permeabilization. For lysosome colocalization experiments, cells expressing LC3-GFP or NBR1-GFP were washed with PBST, fixed with 4% paraformaldehyde at room temperature for 15 minutes, permeabilized with 0.3% TrtionX-100 at room temperature for 10 minutes, and then blocked with 5% goat serum at room temperature for 1 hour. After blocking, cells were then incubated with primary antibodies at 4°C overnight. After washing with PBST, slides were incubated with Alexa Fluor 488/594/647–conjugated secondary antibody (Thermo Fisher Scientific) at room temperature for 1 hour. Sections were counterstained with DAPI (Thermo Fisher Scientific)

and mounted with ProLong Diamond Antifade Mountant (Thermo Fisher Scientific). Fluorescent images were obtained with an Olympus FV3000 and a Zeiss LSM 800 scanning confocal microscope. For colocalization analysis, intracellular puncta were selected and analyzed using the JACoP plugin of ImageJ software. Detailed information on antibodies is listed in Supplementary Table S3.

Flow Cytometry

Flow cytometry was performed as previously described with modifications (67). For *in vivo* sample preparation, mouse tumor tissues were minced with scissors into small pieces and digested at 37°C for 30 minutes with 1 mg/mL Collagenase type IV (Thermo Fisher Scientific) and 0.1 mg/mL DNase I (Roche). Digestion was stopped by EDTA, and cells were filtered through 40-μm cell strainers and then washed twice with staining buffer (PBS supplemented with 1 mmol/L EDTA and 2% FBS). Red blood cells were lysed with ACK lysis buffer (Solarbio) for 5 minutes. Samples were centrifuged and resuspended in staining buffer and stained with a Zombie Aqua fixable viability kit (BioLegend) following the manufacturer's instructions. Around 2×10^6 cells per sample were then washed and incubated with anti-CD16/CD32 (2.4G2, BD Biosciences) in PBS staining buffer for 15 minutes on ice and then stained with the following fluorochrome-labeled antibodies on ice for 1 hour, including anti-CD45 (30-F11), anti-CD11b (M1/70), anti-CD11c (N418), anti-F4/80 (BM8), anti-Ly6C (HK1.4), anti-Ly6G (1A8), anti-IA/IE (M5/114 15.2, BD Biosciences), anti-CD3ε (145–2C11), anti-CD4 (RM4–5), anti-CD8α (53–6.7), anti-CD69 (H1.2F3), anti-H2 (M1/42), anti-CD107α (1D4B), anti–PD-1 (29F.1A12), anti-TIGIT (GIGD7, Invitrogen), anti-TIM3 (RMT3–23), anti-LAG3 (C9B7W, Invitrogen), anti-CD44 (IM7), anti-CD62 L (MEL-14), anti-EpCAM (G8.8), anti-NK1.1 (PK136), anti-CD103 (2E7), anti-CD206 (C068C2), and anti-Gr1 (RB6–8C5). For *in vitro* cell lines, human and mouse PDAC cells were pretreated with ponatinib, GSK583, or DMSO for 24 hours, and then stimulated with IFNγ for 24 hours following staining with antibodies against class I HLA (W6/32), H2 (M1/42), and PD-L1 (29E.2A3 or 10F.9G2). For assessment of cell death, cells were stained with Annexin V and propidium iodide (BioLegend) according to the manufacturer's instructions. Stained cells were analyzed on a BD LSR Fortessa flow cytometer using FACS Diva software and data were analyzed and illustrated by using FlowJo software (BD Biosciences). All antibodies were obtained from BioLegend unless otherwise noted. Detailed information on antibodies is listed in Supplementary Table S3.

Tumor-infiltrating T Cells In Vitro *Restimulation*

To assess the functionality of PDAC-infiltrating lymphocytes *ex vivo*, mouse tumor tissues were collected and dissociated into single-cell suspensions as mentioned in flow cytometry. Dissociated single cells were cultured in the presence of phorbol 12-myristate 13-acetate (100 nmol/L) and ionomycin (1 μmol/L) for 4 hours. BFA (5 μg/mL, BioLegend) was added 2 hours before cell collection to block cytokine secretion. After washing, cells were blocked with anti-CD16/CD32 (2.4G2, BD Biosciences) in PBS staining buffer for 20 minutes on ice followed by staining with antibodies against surface markers as mentioned above. Cells were then fixed with BD fixation/permeabilization solution on ice for 15 minutes and then washed twice with BD Perm/Wash Buffer, followed by intracellular staining with the following antibodies on ice for 1 hour, including anti-IFNγ (XMG1.2), anti-TNFα (MP6-XT22), and anti-GZMB (QA18A28). Detailed information on antibodies is listed in Supplementary Table S3.

T-cell Coculture Assay

KC6141-OVA, KPC^{mut}-OVA, and KPC^{flox}-OVA were seeded into a 96-well plate with RPMI1640 complete medium and preincubated for 2 hours. Naïve OT-I CD8$^+$ T cells were isolated from the spleens of OT-I mice using EasySep Mouse CD8$^+$ T Cell Isolation Kit (StemCell Technologies). Purified CD8$^+$ T cells were cocultured with tumor cells at a ratio of 2.5:1 for 24 hours in RPMI1640 containing 50 U/mL IL2 (PeproTech), 10% FBS, 10 mmol/L HEPES, 100 mmol/L NEAA, and 50 mmol/L β-Mercaptoethanol. BFA (5 μg/mL, BioLegend) was added 2 hours before cell collection to block cytokine secretion. T cells were washed and resuspended in a staining buffer and stained with anti-CD8a and anti-CD69 antibodies for 30 minutes on ice, followed by intracellular staining as described above.

For T-cell proliferation assay, OVA-expressing tumor cells were seeded into a 96-well plate and incubated with either anti-H-2K^b-SIINFEKL antibody (25-D1.16, 100 μg/mL) or IgG control for 30 minutes at 4°C. Isolated CD8$^+$ T cells were labeled with 10 μmol/L CFSE (BioLegend) for 10 minutes at room temperature in the dark and washed three times with RPMI1640 supplemented with 10% FBS. CSFE-labeled CD8$^+$ T cells were cocultured with tumor cell at a ratio of 2.5:1 in complete media. After 48 hours, cells were harvested, and CD8$^+$ T-cell proliferation was analyzed by CFSE dilution using flow cytometry.

For the T-cell killing assay, lymphocytes were obtained from lymph nodes of OT-I mice and seeded in a U-bottom 96-well plate precoated with 5 mg/mL anti-CD3 plus 5 mg/mL anti-CD28 antibodies (BioLegend) in a U-bottom plate for 4–6 days. KC6141-OVA, KPC^{mut}-OVA, and KPC^{flox}-OVA cells (~1×10^5) were seeded into wells of a 96-well plate with a complete medium, and the activated T cells were added. Dead tumor cells were quantified by LDH Cytotoxicity Assay Kit (Beyotime) or Luciferase Reporter Assay Kit (Yeasen) after coculturing for 6 hours. There are three to four cell culture replicates for each condition.

Mouse Experiments

For the subcutaneous model, age-matched 6- to 8-week-old wild-type C57BL/6J or nude mice were used. When they reached 70%–80% confluence, mouse PDAC cells were washed, harvested, and resuspended in PBS. Around 2.5×10^5 cells resuspended in 100 μL PBS were subcutaneously injected into the flank of C57BL/6 or nude mice. Tumor size was measured every 3–4 days using calipers to collect maximal tumor length and width. Tumor volume was measured by length and width and calculated as tumor volume = (length × width^2)/2.

To evaluate the role of specific subsets of T cells in mice, we depleted CD4$^+$ T cells or CD8$^+$ T cells as previously described (66). Mice were pretreated with 150 μg of intraperitoneally injected anti-CD4 antibody (clone GK1.5) or 100 μg of anti-CD8α antibody (clone 2.43), respectively, 3 days before tumor inoculation. Equal amounts of IgG isotype antibodies were injected as a control. After tumor implantation, mice were further treated every 3 days sustained throughout tumor progression. Depletion efficiency was verified by flow cytometry on cheek bleeds on day 14 or spleen at endpoint.

Age-matched 6- to 8-week-old wild-type C57BL/6J were used in orthotopic mouse models. Orthotopic PDAC tumors were established by surgical implantation, as previously described (68). Around 2.5×10^5 cells resuspended in 50 μL PBS were surgically implanted into the pancreas with a 30-gauge insulin syringe. One week after tumors were established *in vivo*, we monitored tumor progression by palpation or ultrasound weekly. To study the antitumor effect of RIPK2 inhibitors, mice were randomized into four different treatment groups when the maximum tumor length reached ~5.0 mm, including (i) vehicle + IgG; (ii) RIPK2i + IgG; (iii) vehicle + anti–PD-1; and (iv) RIPK2i + anti–PD-1. Ponatinib was dissolved in in 0.5% sodium carboxymethyl cellulose (CMC-Na) as previously described and given orally using a gavage needle daily (20 mg/kg). GSK583 was dissolved in 0.5% CMC-Na and given orally with a dose of 10 mg/kg daily. For immune checkpoint blockade experiments, mice received intraperitoneal injection of anti-mouse PD-1 antibody (200 μg, clone RMP1–14, BioXCell) or rat IgG2a isotype control every 3 days. Tumor progression was monitored by palpation or ultrasound weekly. Mice

were euthanized when they met the institutional euthanasia criteria for tumor size (15 mm in diameter) and overall health condition. Tumor weights were measured at the study endpoints after mice were euthanized.

scRNA-seq

Mouse PDAC tumors were isolated after removal of normal tissues. Fresh tumor tissues were washed with HBSS buffer twice, minced and dissociated to single-cell suspensions as mentioned above. Tumor-infiltrating leukocytes were isolated from shNT and shRipk2 tumors using CD45 MicroBeads (Miltenyi Biotec) and cell viability was evaluated microscopically with Trypan Blue. Single-cell suspensions (2×10^5 cells/mL) with PBS were loaded onto microwell chip using the Singleron Matrix Single Cell Processing System. Barcoding Beads are subsequently collected from the microwell chip, followed by reverse transcription of the mRNA captured by the Barcoding Beads and to obtain cDNA and PCR amplification. The amplified cDNA is then fragmented and ligated with sequencing adapters. The scRNA-seq libraries were constructed according to the protocol of the Gexscope Single Cell RNA Library Kits (Singleron). Individual libraries were diluted to 4 nmol/L, pooled, and sequenced on Illumina Novaseq 6000 with 150-bp paired end reads.

scRNA-seq Data Analysis

After acquisition of digital gene expression matrices generated per sample using CeleScope pipeline, preprocessing was conducted to complete quality control using the R package Seurat (v4.3.0) with default parameters. Cell with less than 500 unique molecular identifiers, 250 detected genes, and >5% of reads mapping to mitochondrial RNA were removed. To identify potential doublets, the doublet score was calculated for each cell by Python package Scrublet (v0.2.3) and R package doubletFinder (v2.0). WT and KD groups were normalized respectively and merged together. For batch correction and data integration, 2,000 of the most variable genes were calculated using the SelectIntegrationFeatures function, and all common ambient RNA contaminant genes were removed from integration features, including immunoglobulin genes, T-cell receptor genes, ribosome-protein-coding genes, mitochondrial genes, as well as cell cycle–associated genes. And the resulting ~1,500 genes were used for downstream integration using CCA algorithm by default parameters, followed by principal component analysis (top 30 PCs), graph-based clustering, and UMAP. Default Wilcoxon rank-sum test was used by running FindAllMarkers function in Seurat to find differentially expressed genes (DEG) in each cluster. Annotation of the resulting clusters to cell types was based on the expression of marker genes. We performed a second round of clustering after removing a low-quality cluster (low nFeature_RNA and nCount_RNA, high expression of mitochondrial genes and ribosome-protein-coding genes), a doublet cluster (T cell and monocyte), and two small contaminant $CD45^-$ clusters and performed similar clustering and annotation approach. Finally, we identified a total of 14 cell clusters in 29,448 cells. Next, we filtered T-cell subclustering, and applied a similar strategy as mentioned above.

We performed Slingshot (v2.6.0) to analyze pseudo-time distribution in scRNA-seq data and construct cell trajectories to discover cell-state transitions in $CD8^+$ T cells. PCA-based dimension reduction was performed on DEGs of each phenotype, followed by two-dimensional visualization on UMAP. We selected naïve T cells as a root state when calculating the trajectories and the pseudotime. And $CD8^+$ T cells were split into two lineages. We applied Wilcoxon rank-sum test by running FindAllMarkers and FindMarkers function in Seurat to find DEGs in between KD group and WT group in T-cell, macrophage, and neutrophil subclusters. Then, we chose RACTOME ("CP") gene sets from MsigDB. We ordered the DEGs by Log_2FC and wrapped them into the gene sets for enrichment analysis using R package fgsea (v1.24.0). We calculated module scores for signatures (*Pdcd1, Ctla4, Tigit, Tox, Entpd1, Havcr2, Lag3, Dusp4*, and *Btla*) with Seurat function AddModuleScore per cell and compared the difference between KD and WT group.

PDAC Tissue Analysis and IHC

Human PDAC tissue microarrays were obtained from Zhejiang University Cancer Center Biobank, including 60 pancreatic tumor samples and 10 adjacent normal tissue samples. Human studies were approved by the Ethics Committee of the Second Affiliated Hospital, and prior informed consent was obtained from all subjects under protocol I2021001546. Written informed consent was obtained prior to acquisition of tissue from all patients. The studies were conducted in accordance with ethical guidelines (Declaration of Helsinki). Tissue samples were deparaffinized, rehydrated, and antigen retrieved using the standard IHC protocol. After blocking for 1 hour at room temperature in blocking buffer (5% goat serum in TBST), slides were incubated overnight in a humidified chamber at 4°C with anti-mouse/human antibodies listed in Supplementary Table S4. The stained samples were imaged using Olympus BX61 and VS200 slide scanners, and ImageJ software was used for image visualization and data analysis. The intensity of tissue sections was visually scored in a "anonymized" manner by two pathologists using a scoring system from 0 to 3 (0 = no signal, 1 = weak signal, 2 = intermediate signal, and 3 = strong signal). Image analysis was performed by thresholding for positive staining and normalizing to the total tissue area using ImageJ software (NIH, Bethesda, MD).

Statistical Analysis

Statistical analysis was performed using Graphpad Prism 7. Results are expressed as mean ± SD unless otherwise indicated. Student *t* test (unpaired, two-tailed) was used to compare two groups of independent samples. In an unpaired *t* test, we assumed equal variance and that no samples were excluded from the analysis. ANOVA was used for multivariate comparisons, where indicated. Survival analysis was done using the Kaplan–Meier method, as assessed using a log-rank Mantel–Cox test. $P < 0.05$ was considered statistically significant.

Data Availability

The scRNA-seq data from mouse PDAC for this study have been deposited at National Genomics Data Center under GSA: CRA011762 (https://ngdc.cncb.ac.cn/gsa/), and processed data of scRNA have been deposited at NGDC under OMIX: OMIX004493 (https://ngdc.cncb.ac.cn/omix/).

Authors' Disclosures

J. Qian reports grants from National Natural Science Foundation of China and grants from Zhejiang Province Natural Science Fund for Excellent Young Scholars during the conduct of the study and grants from National Natural Science Foundation of China and grants from Zhejiang Province Natural Science Fund for Excellent Young Scholars outside the submitted work. D. Wang reports grants from the National Natural Science Foundation of China during the conduct of the study. Y. Liu reports grants from National Natural Science Foundation of China and grants from Leading Innovative, Entrepreneur Team Introduction Program of Zhejiang Province during the conduct of the study. No other disclosures were reported.

Authors' Contributions

W. Sang: Data curation, formal analysis, methodology, validation, investigation, writing–review and editing. **Y. Zhou:** Data curation, software, formal analysis, validation, methodology. **H. Chen:** Resources, data curation, investigation, visualization, methodology. **C. Yu:** Software, formal analysis, validation, methodology. **L. Dai:**

Data curation, investigation, methodology. **Z. Liu:** Data curation, methodology. **L. Chen:** Data curation, methodology. **Y. Fang:** Data curation, methodology. **P. Ma:** Data curation, methodology. **X. Wu:** Data curation, methodology. **H. Kong:** Data curation, methodology. **W. Liao:** Resources, writing–review and editing. **H. Jiang:** Conceptualization, resources, supervision, funding acquisition, writing–review and editing. **J. Qian:** Conceptualization, resources, supervision, funding acquisition, writing–review and editing. **D. Wang:** Conceptualization, resources, supervision, funding acquisition, writing–review and editing. **Y. Liu:** Conceptualization, data curation, supervision, funding acquisition, validation, investigation, writing–original draft, project administration, writing–review and editing.

Acknowledgments

This work was supported by National Natural Science Foundation of China (82072615 and 82273274, to Y. Liu; 82173150, to J. Qian; 82303951, to D. Wang; and 82073158, to H. Jiang) and Leading Innovative, Entrepreneur Team Introduction Program of Zhejiang (2019R01007, to Y. Liu) and Zhejiang Province Natural Science Fund for Excellent Young Scholars (LR22H160004, to J. Qian). We thank X. Lu (University of Notre Dame) for proofreading the manuscript and helpful discussion. We thank S.K. Batra (University of Nebraska), C. Yee and Y. Ma (MD Anderson Cancer Center, Houston, TX), and Q. Sun, K. Ding, X. Zeng, M. Lai, J. Shao, T. Liang, H. Zhang, L. Lu, Q. Zhang, X. Wang, and D. Neculai (all from Zhejiang University, Zhejiang, China) for providing experimental materials or technical assistance. We acknowledge the Core Facilities of Zhejiang University School of Medicine (Y. Huang and Y. Li) for technical assistance.

The publication costs of this article were defrayed in part by the payment of publication fees. Therefore, and solely to indicate this fact, this article is hereby marked "advertisement" in accordance with 18 USC section 1734.

Note

Supplementary data for this article are available at Cancer Discovery Online (http://cancerdiscovery.aacrjournals.org/).

Received May 30, 2023; revised August 31, 2023; accepted October 10, 2023; published first October 12, 2023.

REFERENCES

1. Wood LD, Canto MI, Jaffee EM, Simeone DM. Pancreatic cancer: pathogenesis, screening, diagnosis, and treatment. Gastroenterology 2022;163:386–402.
2. Mizrahi JD, Surana R, Valle JW, Shroff RT. Pancreatic cancer. Lancet 2020;395:2008–20.
3. Vesely MD, Zhang T, Chen L. Resistance mechanisms to Anti-PD cancer immunotherapy. Annu Rev Immunol 2022;40:45–74.
4. Hosein AN, Dougan SK, Aguirre AJ, Maitra A. Translational advances in pancreatic ductal adenocarcinoma therapy. Nat Cancer 2022;3:272–86.
5. Ullman NA, Burchard PR, Dunne RF, Linehan DC. Immunologic strategies in pancreatic cancer: making cold tumors hot. J Clin Oncol 2022;40:2789–805.
6. Salas-Benito D, Pérez-Gracia JL, Ponz-Sarvisé M, Rodriguez-Ruiz ME, Martínez-Forero I, Castañón E, et al. Paradigms on immunotherapy combinations with chemotherapy. Cancer Discov 2021;11:1353–67.
7. Bear AS, Vonderheide RH, O'Hara MH. Challenges and opportunities for pancreatic cancer immunotherapy. Cancer Cell 2020;38:788–802.
8. Yamamoto K, Venida A, Yano J, Biancur DE, Kakiuchi M, Gupta S, et al. Autophagy promotes immune evasion of pancreatic cancer by degrading MHC-I. Nature 2020;581:100–5.
9. Alexandrov LB, Nik-Zainal S, Wedge DC, Aparicio SA, Behjati S, Biankin AV, et al. Signatures of mutational processes in human cancer. Nature 2013;500:415–21.
10. Jongsma MLM, Neefjes J, Spaapen RM. Playing hide and seek: Tumor cells in control of MHC class I antigen presentation. Mol Immunol 2021;136:36–44.
11. Byrne KT, Vonderheide RH. CD40 stimulation obviates innate sensors and drives T cell immunity in cancer. Cell Rep 2016;15:2719–32.
12. Freed-Pastor WA, Lambert LJ, Ely ZA, Pattada NB, Bhutkar A, Eng G, et al. The CD155/TIGIT axis promotes and maintains immune evasion in neoantigen-expressing pancreatic cancer. Cancer Cell 2021;39:1342–60.
13. Mezzadra R, Sun C, Jae LT, Gomez-Eerland R, de Vries E, Wu W, et al. Identification of CMTM6 and CMTM4 as PD-L1 protein regulators. Nature 2017;549:106–10.
14. Dersh D, Phelan JD, Gumina ME, Wang B, Arbuckle JH, Holly J, et al. Genome-wide screens identify lineage- and tumor-specific genes modulating MHC-I- and MHC-II-restricted immunosurveillance of human lymphomas. Immunity 2021;54:116–31.
15. Gu SS, Zhang W, Wang X, Jiang P, Traugh N, Li Z, et al. Therapeutically increasing MHC-I expression potentiates immune checkpoint blockade. Cancer Discov 2021;11:1524–41.
16. Burr ML, Sparbier CE, Chan KL, Chan YC, Kersbergen A, Lam EYN, et al. An evolutionarily conserved function of polycomb silences the MHC class I antigen presentation pathway and enables immune evasion in cancer. Cancer Cell 2019;36:385–401.
17. Lawson KA, Sousa CM, Zhang X, Kim E, Akthar R, Caumanns JJ, et al. Functional genomic landscape of cancer-intrinsic evasion of killing by T cells. Nature 2020;586:120–6.
18. Griffin GK, Wu J, Iracheta-Vellve A, Patti JC, Hsu J, Davis T, et al. Epigenetic silencing by SETDB1 suppresses tumour intrinsic immunogenicity. Nature 2021;595:309–14.
19. Wang X, Tokheim C, Gu SS, Wang B, Tang Q, Li Y, et al. In vivo CRISPR screens identify the E3 ligase Cop1 as a modulator of macrophage infiltration and cancer immunotherapy target. Cell 2021;184:5357–74.
20. Manguso RT, Pope HW, Zimmer MD, Brown FD, Yates KB, Miller BC, et al. In vivo CRISPR screening identifies Ptpn2 as a cancer immunotherapy target. Nature 2017;547:413–8.
21. Dubrot J, Du PP, Lane-Reticker SK, Kessler EA, Muscato AJ, Mehta A, et al. In vivo CRISPR screens reveal the landscape of immune evasion pathways across cancer. Nat Immunol 2022;23:1495–506.
22. Pan D, Kobayashi A, Jiang P, Ferrari de Andrade L, Tay RE, Luoma AM, et al. A major chromatin regulator determines resistance of tumor cells to T cell-mediated killing. Science 2018;359:770–5.
23. Morgens DW, Wainberg M, Boyle EA, Ursu O, Araya CL, Tsui CK, et al. Genome-scale measurement of off-target activity using Cas9 toxicity in high-throughput screens. Nat Commun 2017;8:15178.
24. He S, Wang X. RIP kinases as modulators of inflammation and immunity. Nat Immunol 2018;19:912–22.
25. Hofmann SR, Girschick L, Stein R, Schulze F. Immune modulating effects of receptor interacting protein 2 (RIP2) in autoinflammation and immunity. Clin Immunol 2021;223:108648.
26. Torres MP, Rachagani S, Souchek JJ, Mallya K, Johansson SL, Batra SK. Novel pancreatic cancer cell lines derived from genetically engineered mouse models of spontaneous pancreatic adenocarcinoma: applications in diagnosis and therapy. PLoS One 2013;8:e80580.
27. Ma Y, Li J, Wangh CY, Kingsley CV, Fry D, et al. Combination of PD-1 inhibitor and OX40 agonist induces tumor rejection and immune memory in mouse models of pancreatic cancer. Gastroenterology 2020;159:306–19.
28. Ijichih CA, Gorska AE, Aakre ME, Fujitani Y, Fujitani S, et al. Aggressive pancreatic ductal adenocarcinoma in mice caused by pancreas-specific blockade of transforming growth factor-beta signaling in cooperation with active Kras expression. Genes Dev 2006;20:3147–60.
29. Peng J, Sun BF, Chen CY, Zhou JY, Chen YS, Chen H, et al. Single-cell RNA-seq highlights intra-tumoral heterogeneity and malignant progression in pancreatic ductal adenocarcinoma. Cell Res 2019;29:725–38.
30. Peih LL, Fridley BL, Jenkins GD, Kalari KR, Lingle W, et al. FKBP51 affects cancer cell response to chemotherapy by negatively regulating Akt. Cancer Cell 2009;16:259–66.

31. Moffitt RA, Marayati R, Flate EL, Volmar KE, Loeza SG, Hoadley KA, et al. Virtual microdissection identifies distinct tumor- and stroma-specific subtypes of pancreatic ductal adenocarcinoma. Nat Genet 2015;47:1168–78.
32. Yingh KAC, Lyssiotis CA, Hua S, Chu GC, Fletcher-Sananikone E, et al. Oncogenic Kras maintains pancreatic tumors through regulation of anabolic glucose metabolism. Cell 2012;149:656–70.
33. Qian J, Olbrecht S, Boeckx B, Vosh LD, Etlioglu E, et al. A pan-cancer blueprint of the heterogeneous tumor microenvironment revealed by single-cell profiling. Cell Res 2020;30:745–62.
34. Goncharov T, Hedayati S, Mulvihill MM, Izrael-Tomasevic A, Zobel K, Jeet S, et al. Disruption of XIAP-RIP2 association blocks NOD2-mediated inflammatory signaling. Mol Cell 2018;69:551–65.
35. Panda S, Gekara NO. The deubiquitinase MYSM1 dampens NOD2-mediated inflammation and tissue damage by inactivating the RIP2 complex. Nat Commun 2018;9:4654.
36. Zehn D, Thimme R, Lugli E, de Almeida GP, Oxenius A. 'Stem-like' precursors are the fount to sustain persistent CD8(+) T cell responses. Nat Immunol 2022;23:836–47.
37. Falcomatà C, Bärthel S, Schneider G, Rad R, Schmidt-Supprian M, Saur D. Context-specific determinants of the immunosuppressive tumor microenvironment in pancreatic cancer. Cancer Discov 2023;13:278–97.
38. Buquicchio FA, Satpathy AT. Interrogating immune cells and cancer with CRISPR-Cas9. Trends Immunol 2021;42:432–46.
39. Cucolo L, Chen Q, Qiu J, Yu Y, Klapholz M, Budinich KA, et al. The interferon-stimulated gene RIPK1 regulates cancer cell intrinsic and extrinsic resistance to immune checkpoint blockade. Immunity 2022;55:671–85.
40. Honjoh WT, Kamata K, Minaga K, Kudo M. RIPK2 as a new therapeutic target in inflammatory bowel diseases. Front Pharmacol 2021;12:650403.
41. Li D, Tang L, Liu B, Xu S, Jin M, Bo W. RIPK2 is an unfavorable prognosis marker and a potential therapeutic target in human kidney renal clear cell carcinoma. Aging 2021;13:10450–67.
42. Yang Q, Tian S, Liu Z, Dong W. Knockdown of RIPK2 inhibits proliferation and migration, and induces apoptosis via the NF-κB signaling pathway in gastric cancer. Front Genet 2021;12:627464.
43. Li G, Xu Z, Peng J, Yan Y, Liu Y, Zhang X, et al. The RIPK family: expression profile and prognostic value in lung adenocarcinoma. Aging 2022;14:5946–58.
44. Yan Y, Zhou B, Qian C, Vasquez A, Kamra M, Chatterjee A, et al. Receptor-interacting protein kinase 2 (RIPK2) stabilizes c-Myc and is a therapeutic target in prostate cancer metastasis. Nat Commun 2022;13:669.
45. Wang W, Marinis JM, Beal AM, Savadkar S, Wu Y, Khan M, et al. RIP1 kinase drives macrophage-mediated adaptive immune tolerance in pancreatic cancer. Cancer Cell 2018;34:757–74.
46. Dersh D, Hollý J, Yewdell JW. A few good peptides: MHC class I-based cancer immunosurveillance and immunoevasion. Nat Rev Immunol 2021;21:116–28.
47. Blander JM. Regulation of the cell biology of antigen cross-presentation. Annu Rev Immunol 2018;36:717–53.
48. Gettinger S, Choi J, Hastings K, Truini A, Datar I, Sowell R, et al. Impaired HLA class I antigen processing and presentation as a mechanism of acquired resistance to immune checkpoint inhibitors in lung cancer. Cancer Discov 2017;7:1420–35.
49. McGranahan N, Rosenthal R, Hiley CT, Rowan AJ, Watkins TBK, Wilson GA, et al. Allele-specific HLA loss and immune escape in lung cancer evolution. Cell 2017;171:1259–71.
50. Jhunjhunwala S, Hammer C, Delamarre L. Antigen presentation in cancer: insights into tumour immunogenicity and immune evasion. Nat Rev Cancer 2021;21:298–312.
51. Ryschich E, Nötzel T, Hinz U, Autschbach F, Ferguson J, Simon I, et al. Control of T-cell-mediated immune response by HLA class I in human pancreatic carcinoma. Clin Cancer Res 2005;11(2 Pt 1):498–504.
52. Pommier A, Anaparthy N, Memos N, Kelley ZL, Gouronnec A, Yan R, et al. Unresolved endoplasmic reticulum stress engenders immune-resistant, latent pancreatic cancer metastases. Science 2018;360:eaao4908.
53. Waddell N, Pajic M, Patch AM, Chang DK, Kassahn KS, Bailey P, et al. Whole genomes redefine the mutational landscape of pancreatic cancer. Nature 2015;518:495–501.
54. Scarpa A, Chang DK, Nones K, Corbo V, Patch AM, Bailey P, et al. Whole-genome landscape of pancreatic neuroendocrine tumours. Nature 2017;543:65–71.
55. Cheung PF, Yang J, Fang R, Borgers A, Krengel K, Stoffel A, et al. Progranulin mediates immune evasion of pancreatic ductal adenocarcinoma through regulation of MHCI expression. Nat Commun 2022;13:156.
56. Lupfer C, Thomas PG, Anand PK, Vogel P, Milasta S, Martinez J, et al. Receptor interacting protein kinase 2-mediated mitophagy regulates inflammasome activation during virus infection. Nat Immunol 2013;14:480–8.
57. Irving AT, Mimuroh KTA, Lo C, Wheeler R, Turner LJ, et al. The immune receptor NOD1 and kinase RIP2 interact with bacterial peptidoglycan on early endosomes to promote autophagy and inflammatory signaling. Cell Host Microbe 2014;15:623–35.
58. Cooney R, Baker J, Brain O, Danis B, Pichulik T, Allan P, et al. NOD2 stimulation induces autophagy in dendritic cells influencing bacterial handling and antigen presentation. Nat Med 2010;16:90–7.
59. Daoud M, Broxtermann PN, Schorn F, Werthenbach JP, Seeger JM, Schiffmann LM, et al. XIAP promotes melanoma growth by inducing tumour neutrophil infiltration. EMBO Rep 2022;23:e53608.
60. Mares A, Miah AH, Smith IED, Rackham M, Thawani AR, Cryan J, et al. Extended pharmacodynamic responses observed upon PROTAC-mediated degradation of RIPK2. Commun Biol 2020;3:140.
61. Kobayashi K, Inohara N, Hernandez LD, Galán JE, Núñez G, Janeway CA, et al. RICK/Rip2/CARDIAK mediates signalling for receptors of the innate and adaptive immune systems. Nature 2002;416:194–9.
62. Miah AH, Smith IED, Rackham M, Mares A, Thawani AR, Nagilla R, et al. Optimization of a series of RIPK2 PROTACs. J Med Chem 2021;64:12978–3003.
63. Hegde S, Krisnawan VE, Herzog BH, Zuo C, Breden MA, Knolhoff BL, et al. Dendritic cell paucity leads to dysfunctional immune surveillance in pancreatic cancer. Cancer Cell 2020;37:289–307.
64. Li F, Huang Q, Luster TA, Huh Z, Ng WL, et al. In vivo epigenetic CRISPR screen identifies Asf1a as an immunotherapeutic target in Kras-mutant lung adenocarcinoma. Cancer Discov 2020;10:270–87.
65. Li W, Xuh XT, Cong L, Love MI, Zhang F, et al. MAGeCK enables robust identification of essential genes from genome-scale CRISPR/Cas9 knockout screens. Genome Biol 2014;15:554.
66. Liu X, Bao X, Hu M, Changh JM, Cheng J, et al. Inhibition of PCSK9 potentiates immune checkpoint therapy for cancer. Nature 2020;588:693–8.
67. Ruscetti M, M JPt, Mezzadra R, Russell J, Leibold J, Romesser PB, et al. Senescence-induced vascular remodeling creates therapeutic vulnerabilities in pancreas cancer. Cell 2020;181:424–41.e21.
68. Aiello NM, Rhim AD, Stanger BZ. Orthotopic injection of pancreatic cancer cells. Cold Spring Harb Protoc 2016;2016:pdb.prot078360.